AGU PUBLICATIONS

JGR

Journal of Geophysical Research: Oceans

RESEARCH ARTICLE

10.1002/2016JC012144

Special Section:
Dense water formations in the North Western Mediterranean: from the physical forcings to the biogeochemical consequences

Scales and dynamics of Submesoscale Coherent Vortices formed by deep convection in the northwestern Mediterranean Sea

Anthony Bosse[1], Pierre Testor[1], Loïc Houpert[2], Pierre Damien[3], Louis Prieur[4], Daniel Hayes[5], Vincent Taillandier[4], Xavier Durrieu de Madron[6], Fabrizio d'Ortenzio[4], Laurent Coppola[4], Johannes Karstensen[7], and Laurent Mortier[8]

[1]Sorbonne Universités (UPMC Univ. Paris 06)-CNRS-IRD-MNHN, UMR 7159, Laboratoire d'Océanographie et de Climatologie, IPSL, Paris, France, [2]Scottish Association for Marine Science, Oban, Argyll, Scotland, [3]Departamento de Oceanografia Fisica, Centro de Investigacion Cientifica y de Educacion Superior de Ensenada, Ensenada, Mexico, [4]Sorbonne Universités (UPMC Univ. Paris 06), UMR 7093, Laboratoire d'Océanographie de Villefranche, Observatoire Océanologique, Villefranche/mer, France, [5]Oceanography Center, University of Cyprus, Nicosia, Cyprus, [6]Centre de Recherche et de Formation sur les Environnements Méditerranéens, CNRS-Université de Perpignan, Perpignan, France, [7]GEOMAR, Helmholtz Zentrum für Ozeanforschung, Kiel, Germany, [8]ENSTA-Paristech, Palaiseau, France

Key Points:
- Small-scale eddies (5–10 km radius) formed by deep convection are described from in situ observations in the NW Mediterranean Sea
- Bottom-reaching convection might favor the formation of cyclonic vortices characterized by surface-intensified or depth-intensified velocities
- Long-lived vortices can transport a significant fraction of the convected waters and influence the convection onset the following winter

Correspondence to:
A. Bosse,
bosse@locean-ipsl.upmc.fr

Citation:
Bosse, A., et al. (2016), Scales and dynamics of Submesoscale Coherent Vortices formed by deep convection in the northwestern Mediterranean Sea, *J. Geophys. Res. Oceans*, *121*, doi:10.1002/2016JC012144.

Received 12 JUL 2016
Accepted 20 SEP 2016
Accepted article online 26 SEP 2016

Abstract Since 2010, an intense effort in the collection of in situ observations has been carried out in the northwestern Mediterranean Sea thanks to gliders, profiling floats, regular cruises, and mooring lines. This integrated observing system enabled a year-to-year monitoring of the deep waters formation that occurred in the Gulf of Lions area during four consecutive winters (2010–2013). Vortical structures remnant of wintertime deep vertical mixing events were regularly sampled by the different observing platforms. These are Submesoscale Coherent Vortices (SCVs) characterized by a small radius (∼5–8 km), strong depth-intensified orbital velocities (∼10–20 cm s^{-1}) with often a weak surface signature, high Rossby (∼0.5) and Burger numbers O(0.5–1). Anticyclones transport convected waters resulting from intermediate (∼300 m) to deep (∼2000 m) vertical mixing. Cyclones are characterized by a 500–1000 m thick layer of weakly stratified deep waters (or bottom waters that cascaded from the shelf of the Gulf of Lions in 2012) extending down to the bottom of the ocean at ∼2500 m. The formation of cyclonic eddies seems to be favored by bottom-reaching convection occurring during the study period or cascading events reaching the abyssal plain. We confirm the prominent role of anticyclonic SCVs and shed light on the important role of cyclonic SCVs in the spreading of a significant amount (∼30%) of the newly formed deep waters away from the winter mixing areas. Since they can survive until the following winter, they can potentially have a great impact on the mixed layer deepening through a local preconditioning effect.

1. Introduction

Only a few particular places of the world's oceans are exposed to very intense atmospheric forcing in winter and have a sufficiently weak open-ocean stratification that allows vertical mixing to reach very great depths (>1500–2000 m). These areas are known to be located in the center of a large-scale cyclonic gyre in the Labrador, the Greenland, the Weddell, and the northwestern Mediterranean Seas [*Killworth*, 1983]. This phenomenon called open-ocean deep convection is of critical importance for the ventilation of the deep oceans and the thermohaline circulation. It has been studied thoroughly since the 1970s (see *Marshall and Schott* [1999] for a review). This phenomenon can be classically described in three different phases as follows [*MEDOC-Group*, 1970]:

1. A preconditioning phase: A basin-scale cyclonic circulation drives a doming of isopycnals at its center which helps the deepening of the mixed layer during events of intense surface buoyancy loss. In addition, mesoscale eddies can also act as local preconditioning agents [*Legg et al.*, 1998; *Lherminier et al.*, 1999].
2. A mixing phase: Cold and dry winds strongly blow over the preconditioned area resulting in intense heat losses at the air-sea interface. During a winter storm, heat losses typically reach several hundreds of watts

per squared meter with peaks close to -1000 W m^{-2} for a couple of days [*Leaman and Schott*, 1991]. In response to this strong atmospheric forcing, the oceanic vertical mixing progressively creates a convective *Mixed Patch* of roughly homogeneous waters with a typical horizontal scale of about 50–100 km. The mixed layer deepens as long as the surface cooling is strong enough. In some places, such as the Gulf of Lions in the northwestern Mediterranean Sea, the mixed layer depth can reach the bottom of the ocean as it has been observed for five consecutive winters from 2009 to 2013(L. Houpert et al., Observation of open-ocean deep convection in the northwestern Mediterranean sea: Seasonal and interannual variability of mixing and deep water masses for the 2007–2013 period, submitted to *Journal of Geophysical Research*, 2016).

3. A spreading phase: When the strong heat losses and evaporation decrease, the restratification of the water column quickly occurs. Potential energy is converted into kinetic energy through the baroclinic instability of the rim-current circling the mixed patch and leads to the formation of mesoscale eddies [*Gascard*, 1978; *Legg and Marshall*, 1993; *Jones and Marshall*, 1997; *Testor and Gascard*, 2006]. The large-scale spreading of the newly formed deep waters out of the convective region is known to involve different processes. In the northwestern Mediterranean Sea, a significant part of the deep waters seems to be incorporated by the "Northern Current" [*Send et al*., 1996], which circles the northern part of the convection zone (see *Millot* [1999] for a review about the circulation of the different water masses of the western Mediterranean Sea). Another important portion of the newly formed deep waters could also get trapped inside very coherent submesoscale eddies responsible for their propagation toward the basin interior as shown by *Testor and Gascard* [2003, 2006]. Recent abrupt changes in the WMDW characteristics have been shown to eventually propagate to Gibraltar in about 3 years, subsequently impacting the Mediterranean overflow [*Schroeder et al*., 2016].

In the 1990s, Lagrangian floats seeded within the mixed patch revealed the role of Submesoscale Coherent Vortices (SCVs) in the spreading of the newly formed deep waters. These structures were found to be able to wander several hundreds of kilometers away from the deep convection zone and be long-lived in the Greenland Sea [*Gascard et al*., 2002], in the Labrador Sea [*Lilly and Rhines*, 2002], and in the western Mediterranean Sea [*Testor and Gascard*, 2003, 2006]. These SCVs are similar to the Local Dynamics Experiment SCVs described by *McWilliams* [1985]. They are isolated and coherent circulation features characterized by a small radius (about 5 km in the northwestern Mediterranean Sea [*Testor and Gascard*, 2006]), an extended lifetime ($>$1 year [*Testor and Gascard*, 2003; *Ronski and Budéus*, 2006]). Their rotation sets transport barriers that drastically reduce the lateral exchanges between their core and the surrounding waters [*Rhines and Young*, 1983; *Provenzale*, 1999]. They are, therefore, extremely efficient in transporting physical and biogeochemical tracers characteristics of their generation site over long distances [*D'Asaro*, 1988a; *Testor and Gascard*, 2003; *Bower et al*., 2013; *L'Hégaret et al*., 2016]. However, due to their small horizontal extension and their little surface signature, a fine-scale description of the SCVs remnant of wintertime convective events, especially along the vertical axis, is still lacking.

In the last decade, glider technology [*Testor et al*., 2010] has been intensively used in the northwestern Mediterranean Sea for repeated cross-basin transects (see Figure 1). By allowing a relatively high horizontal resolution (distance between consecutive profiles $\sim$2–4 km), gliders can dynamically characterize small-scale SCVs [*Martin et al*., 2009; *Fan et al*., 2013; *Pelland et al*., 2013; *Bosse et al*., 2015; *Thomsen et al*., 2016]. In this study, we analyze in situ observations collected from November 2009 to October 2013 by different sampling platforms (see Figure 1): the intense glider sampling of the upper 1000 m of the water column, more than 600 full-depth CTD casts collected during nine basin scale cruises, as well as data from mooring observations from the deep mixing zones of the Gulf of Lions and the Ligurian Sea. This unprecedented collection of in situ observations in a convective region allows the first comprehensive study of the vortical structures responsible for the large-scale spreading of deep convection water masses.

2. Data and Methods

2.1. Hydrographical Data Set

In 2010, a Mediterranean Ocean Observing System for the Environment (MOOSE, http://www.moose-network.fr/) was set up as a multidisciplinary and multiplatform integrated monitoring system of the NW Mediterranean Sea to detect and identify long-term environmental evolution. The present study utilizes

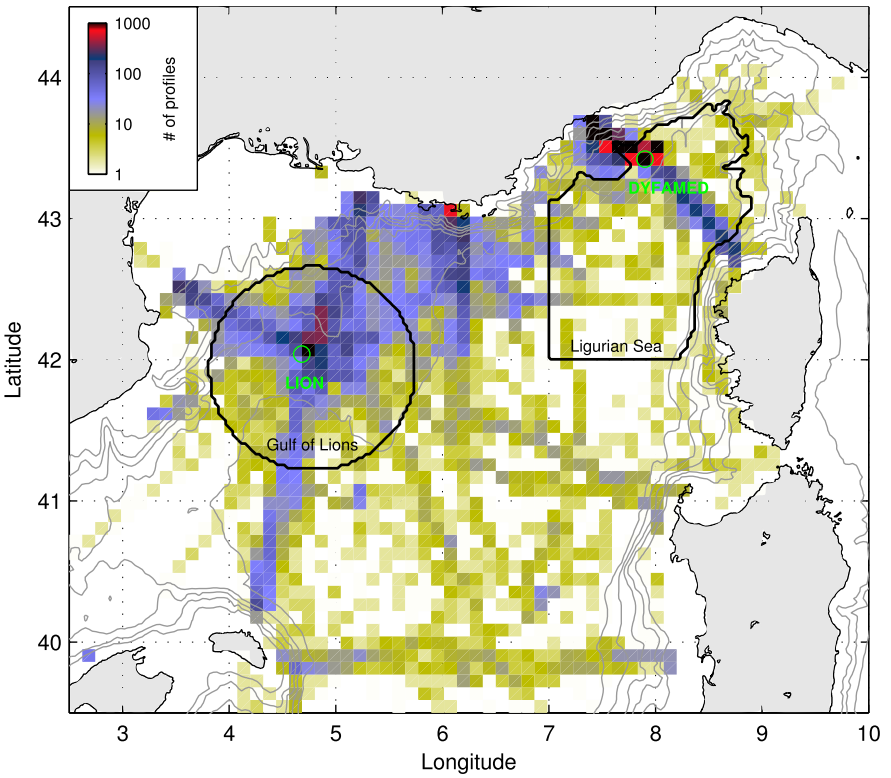

Figure 1. Map of in situ observations density, in number of profiles within 10 km × 10 km bins, carried out in the northwestern Mediterranean Sea during the November 2009–October 2013 period by different platforms (R/Vs, gliders, and Argo floats). The arrows show the mean surface currents forming a basin-scale cyclonic gyre. The name of the main currents is also indicated: the Northern Current (NC), the North-Balearic Front (NBF), and the Western Corsica Current (WCC). The two annotated boxes—"Gulf of Lions" (75 km around 41°55′N–4°45′E) and "Ligurian Sea" (lon. >7°E, lat. >42°, and depth >2300 m)—delineate the two important and contrasted regions regarding the winter mixing. Green circles show the location of the two offshore mooring lines (LION and DYFAMED). Isobaths every 500 m also contoured in light gray.

hydrographical observations from MOOSE (cruises, gliders, and mooring lines) to provide a long-term and multiscale description of the NW Mediterranean Sea. Additional cruises and glider data have been collected in 2012–2013 in the common framework of the dense water formation experiment of the HYMEX and MERMEX programs [*Durrieu de Madron et al.*, 2011; *Drobinski et al.*, 2014].

2.1.1. CTD Casts Collected by R/Vs

Since November 2009, nine basin scale cruises have taken place in the NW Mediterranean Sea (chronologically: MOOSE-GE in May–June 2010 [*Testor and Mortier*, 2010], CASCADE in March 2011 [*Durrieu de Madron*, 2011], MOOSE-GE in June 2011 [*Testor et al.*, 2011], MOOSE-GE in July 2012 [*Testor et al.*, 2012], DOWEX in September 2012 [*Mortier*, 2012], DEWEX in February 2013 [*Testor*, 2013] and in April 2013 [*Conan*, 2013], MOOSE-GE in June–July 2013 [*Testor et al.*, 2013], and DOWEX in September 2013 [*Mortier and Taillandier*, 2013]). Since 2010, each of the MOOSE-GE cruise provides a yearly snapshot in summer of the open-ocean part of the basin with about 70–100 CTD stations. Following a similar strategy, the DOWEX and DEWEX cruises, which take place between the summer cruises, provide the hydrological conditions prior, during and after the 2013 winter convection period. The common key objective of the MOOSE observatory is to monitor the deep waters formation in the Gulf of Lions in order to assess its effect on biogeochemical cycles, and on the longer-term environmental and ecosystemic trends and anomalies.

The conductivity, temperature, and pressure measurements during these cruises have all been performed using a Seabird SBE 911+ CTD probe. The CT sensors have been calibrated by predeployment and postdeployment laboratory analysis. After calibration, the absolute accuracy of the measurements is 0.003 for the salinity and 0.001°C for the temperature. These calibrated CTD casts provide a ground truth for the other instruments such as the deep mooring lines (LION and DYFAMED) and the autonomous underwater gliders and floats (see Figure 1).

2.1.2. The Mooring Lines

The LION mooring line is located approximately in the center of the deep waters formation zone at 42°02′N/4°41′E (bottom depth at 2350 m, see Figure 1). It was equipped from November 2009 to October 2013 with 11 SeaBird Microcats SBE37 (conductivity-temperature-pressure sensor) regularly spaced along the line from 150 to 2300 m. In addition, five Nortek Aquadopp current meters measured horizontal and vertical currents.

An intercalibration of the moorings instruments with the shipborne CTD has been carried out after and before each deployment to ensure the consistency of the hydrographical data set (Houpert et al., submitted manuscript).

The DYFAMED mooring line in the Ligurian Sea (see Figure 1) was equipped with fewer instruments (four SeaBird Microcats SBE37 at about 200, 700, 1000, and 2000 m) and was calibrated in a similar way.

2.1.3. Gliders Data

Gliders are steerable autonomous platforms that sample the ocean along saw-tooth trajectories between the surface and a maximum depth of 1000 m [*Testor et al*., 2010]. As the slopes of isopycnals (a few degrees) are generally much smaller than the glider pitch angle ($\pm$15–30°), dives and ascents can be considered as vertical profiles to some extent. Under this assumption, two consecutive profiles down to 1000 m are separated by approximately 2–4 km and 2–4 h depending on the currents and the sampling strategy of the platform. Sensors can be powered on only during dives or ascents, or both. With a horizontal speed of 30–40 km d^{-1} relative to the water, gliders are perfectly suited to capture balanced circulation features and eddies that propagate at slower speeds. By comparing its dead reckoning navigation and GPS fixes at the surface, they also deduce a current between two surfacings—hereafter referred to as the "depth-average currents" (DAC)—representing the mean currents averaged over each dive. A compass calibration has been carried out before each deployment allowing DAC to be used to reference geostrophic velocities as commonly done in previous studies [*Gourdeau et al*., 2008; *Davis et al*., 2008; *Bouffard et al*., 2010, 2012; *Pietri et al*., 2013; *Høydalsvik et al*., 2013; *Pelland et al*., 2013; *Pietri et al*., 2014; *Bosse et al*., 2015; *Thomsen et al*., 2016].

The very first glider deployments in the northwestern Mediterranean Sea were carried out in 2006. From 2010 on, gliders have been deployed on a regular basis in the framework of the MOOSE project. In this study, we examine the glider profiles collected from November 2009 to October 2013 ($\sim$28,000 profiles to 1000 m).

Gliders were equipped with a pumped or unpumped CTD probe that generally needs to be corrected with an offset as a first order correction for each single deployment. We compared the gliders data with nearby calibrated CTD casts from R/Vs ($<$15 km and $<$3 days), and/or with the calibrated mooring lines LION and DYFAMED ($<$2.5 km and $<$18 h, about the inertial period in this region). The cross-platform hydrographical consistency was checked in the deeper layers sampled by the gliders (700–1000 m) as done in *Bosse et al*. [2015], because the θ/S variability is relatively small at those depths. The deduced θ and S offsets are on average about 0.01°C and 0.01, respectively. If no direct comparison with calibrated data is possible ($\sim$30% of the deployments), only salinity was offset to fit the linear θ/S relationship between the intermediate and deep layers (700–1000 m) and provided by the calibrated data from R/Vs (see Figure 2). In addition, thermal lag error of the unpumped CTD probe that can affect salinity measurements in strong summer thermoclines have been corrected following *Garau et al*. [2011].

This method ensures the glider CTD errors in temperature and salinity to be smaller than, respectively, 0.01°C and 0.01. These numbers are much smaller than the relative variability associated with the vortical structures of interest (order of 0.1 both in temperature and salinity). The overall consistency of the data set is set by the calibrated CTD data from the MOOSE research cruises (previously described in section 2.1.1).

2.1.4. Argo Floats Data

Argo floats are autonomous profiling floats that drift at a given parking depth for a given time period. At the end of their drifting time, they dive to 2000 m and collect a profile of temperature and salinity during the upcast. The collected data are sent in real time to a data center after which they return to their parking depth. For the Mediterranean Sea, the MedArgo program has set the interval between the successive surfacings of Argo floats to 4–5 days and their parking depth to $\sim$400 m, the approximate depth of the Levantine Intermediate Waters [*Poulain et al*., 2007].

We applied the same calibration procedure of the hydrographical data collected by the Argo profiling floats as for the gliders. They collected a total of about 2700 profiles in the northwestern Mediterranean Sea for our

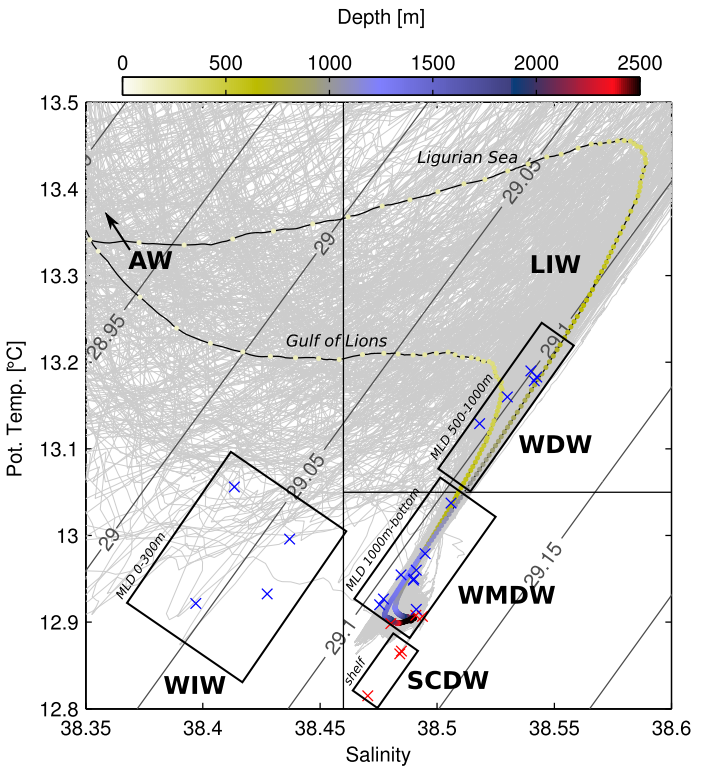

Figure 2. θ/S diagram constructed from all the CTD casts carried out by R/Vs in the open-ocean part of the NW Mediterranean Sea for the November 2009–October 2013 period. The main water masses are annotated: Atlantic Waters (AW), Winter Intermediate Waters (WIW), Winter Deep Waters (WDW), Levantine Intermediate Waters (LIW), Western Mediterranean Deep Waters (WMDW), and Shelf Cascading Dense Waters (SCDW). The slanted lines correspond to density contours. Blue (resp., red) crosses correspond to the θ/S core characteristics of the anticyclonic (resp., cyclonic) eddies. We also represent the mean profiles corresponding to the Gulf of Lions and the Ligurian Sea with colors indicating the depth.

study period. In this study, they are only used to document the water mass properties of the basin, since identifying such small-scale eddies (5–10 km radius, few days periods) is hardly possible due to their too sparse spatiotemporal sampling.

2.2. Vortex Detection and Characterization

The detection and inferred parameters associated with each eddy is somewhat different depending on the platform.

2.2.1. Gliders

Eddies were identified from the rotation measured by the DAC and the isopycnal deformation. An original method is used to characterize submesoscale eddies in cyclogeostrophic balance (see details in Appendix A). Figure 3 shows examples of different eddies sampled by gliders.

2.2.2. R/Vs

Eddies were detected from the isopycnal deformation: anticyclones being characterized by a subsurface weakly stratified layer and cyclones by a doming of deep isopycnals. The distance between two CTD casts during research cruises is usually ∼20–40 km, which cannot resolved the horizontal scales of small-scale eddies. However, shipborne CTD casts still provide crucial information on their vertical structure from the surface to the ocean bottom, thus extending the glider sampling restricted to the first 1000 m. Two examples of anticyclonic and cyclonic eddies sampled by shipborne CTD are shown in Figure 4.

2.2.3. Mooring

Following *Lilly and Rhines* [2002], a method based on the hodograph computed with the five current meters was used to detect eddies passing by the LION mooring line [*Houpert*, 2013]. Indeed, a localized hodograph deflection perpendicular to the mean advection indicates rotational currents. Furthermore, the shape of this deflection documents the distance of the mooring to the eddy center, the eddy radius, and peak velocities. A close inspection of the isopycnal deformation was eventually done to select only the relevant eddies: ones that unambiguously correspond to the vortices category we define hereafter. Examples of two eddies passing by the mooring can be seen in Figure 5.

Tables 1 and 2 sum up the characteristics of the 18 anticyclones and 25 cyclones detected during the study period.

2.3. Dynamical Diagnostics

The vortices radius R is estimated as half the radial distance between two opposite peak velocities. Maximum velocities V_{max} are then coherently defined as the mean of those peak velocities. The Rossby number—defined as $Ro \equiv \nabla\times\mathbf{v_h}/f$ with $\nabla\times$ the curl operator, v_h is the horizontal currents, and f is the Coriolis parameter—is here approximated by $2V_{\mathrm{max}}/fR$. The latter expression is valid for circular eddies in solid body rotation.

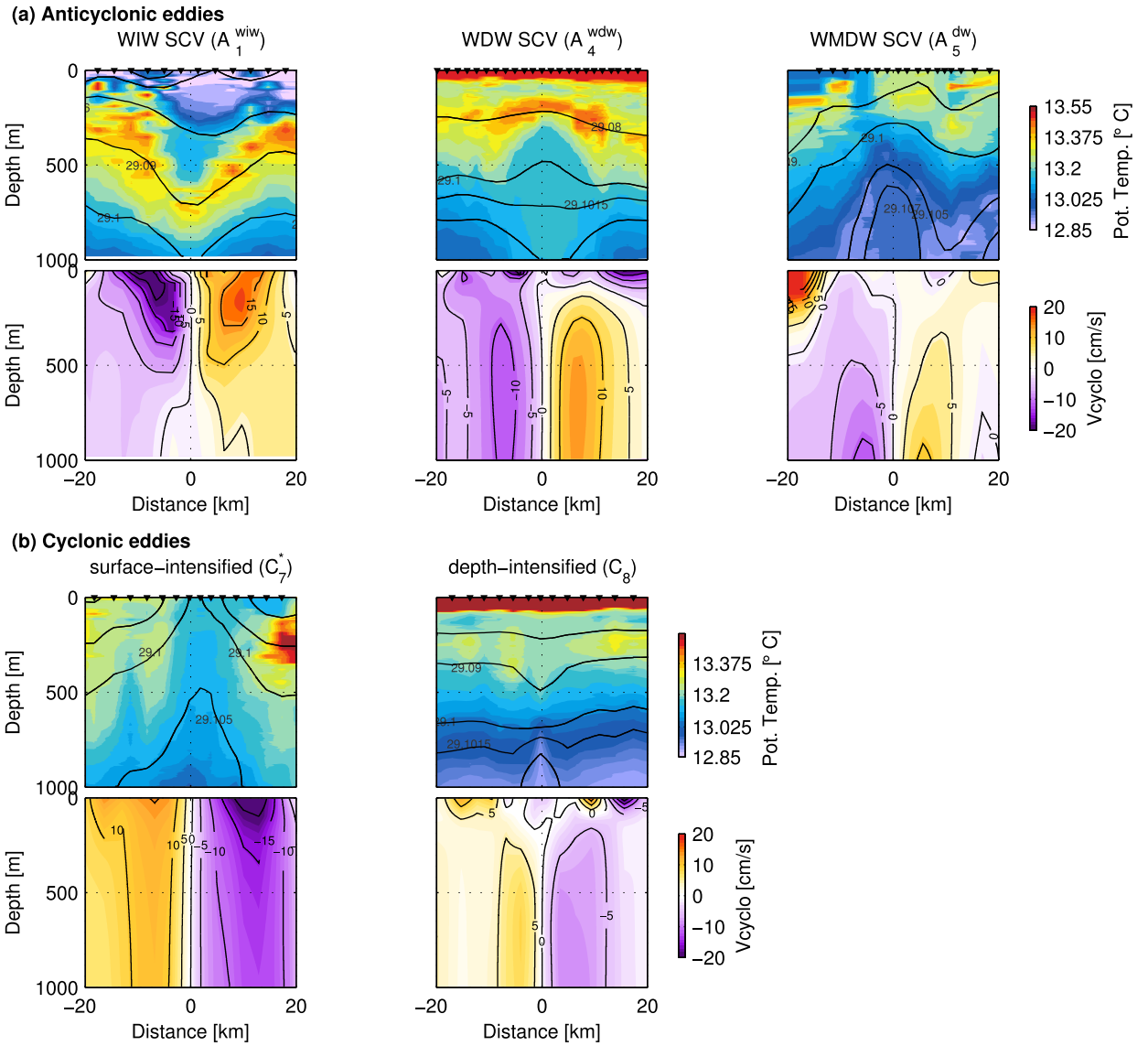

Figure 3. Examples of vortices sampled by gliders: (a) anticyclonic eddy A_1^{wiw} of Winter Intermediate Waters, A_4^{wdw} of Winter Deep Waters and A_5^{dw} of Western Mediterranean Deep Waters; (b) cyclonic eddy C_7^* with surface- and C_8 with depth-intensified orbital velocities. For each eddy, the upper plot represents the cross-track temperature section with isopycnals contours and the lower plot the cyclostrophic orbital velocities across the eddy. The glider sampling is represented by the black triangles.

Anticyclonic SCVs are known to have depth-intensified velocities due to their particular density structure that implies anticyclonic (resp., cyclonic) shear below (resp., above) their core depth where the maximum velocities are observed. All SCVs of WMDW (A_i^{dw} in Table 1) as well as a few depth-intensified cyclonic vortices ($C_{1,3,8}$ in Table 2) have peak velocities located below 1000 m, the maximum depth of the glider sampling. For those eddies, R is estimated at the maximum sampling depth, the eddy radius being unlikely to vary much with depth. However, the orbital peak velocities and Rossby number are obviously underestimated in that case.

The horizontal scale of oceanic eddies is controlled by the internal deformation radius: $R_d \equiv NH/f$ depending on H its vertical extension and N the water column stratification ($N^2 \equiv -g\partial_z\sigma/\rho_0$). The stratification often decreases with depth: in the NW Mediterranean Sea, $N \leq 5f$ below 500 m. This explains why subsurface eddies have a small radius compared to surface mesoscale eddies and are qualified as submesoscale eddies [*McWilliams*, 2016]. Their radius is close to the local deformation radius, whereas surface mesoscale turbulence is characterized by a horizontal scale order of several deformation radius (typically 30–50 km)

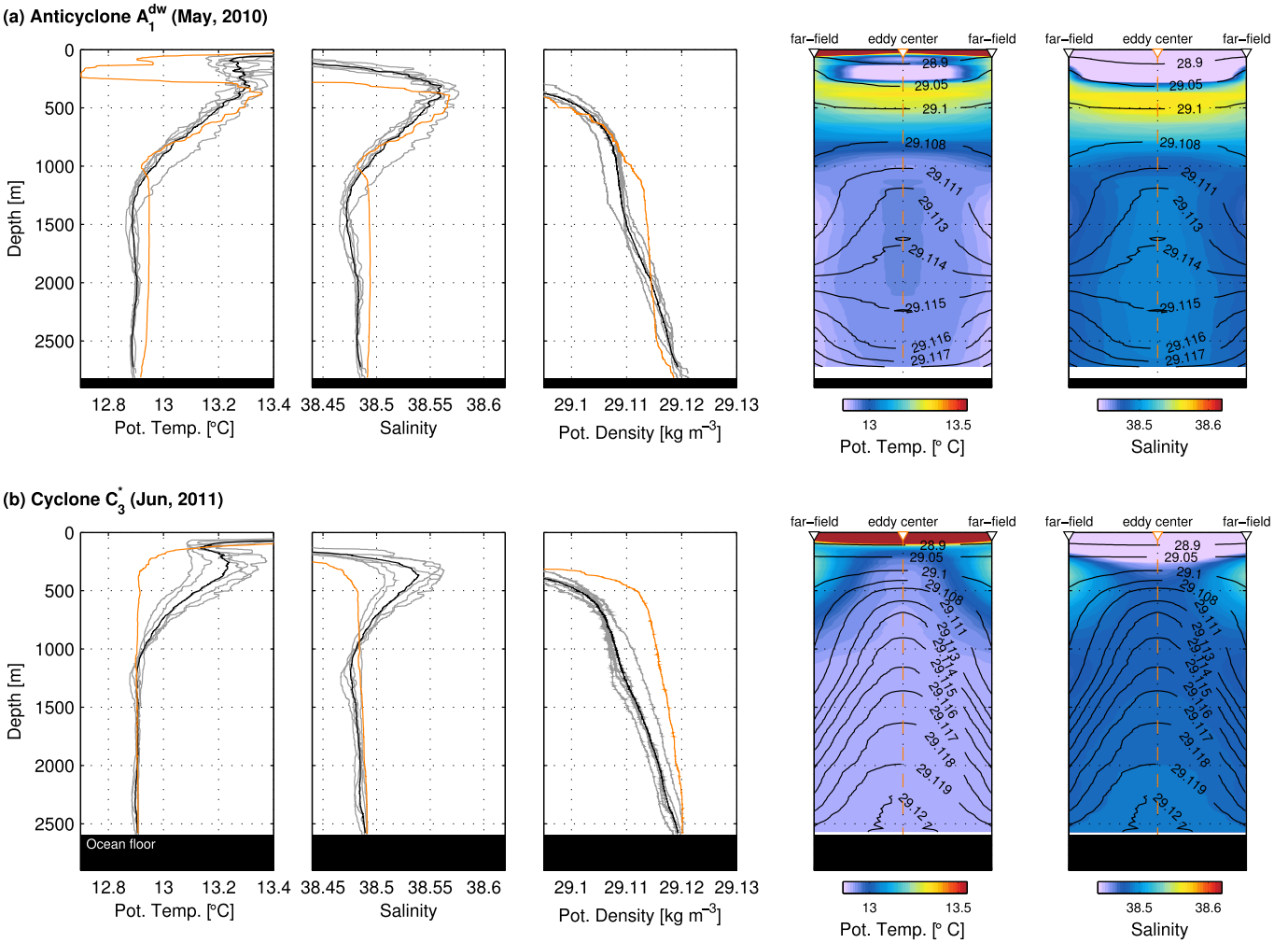

Figure 4. Examples of vortices sampled by shipborne CTD: (a) anticyclonic SCV A_1^{dw} of Western Mediterranean Deep Waters observed in June 2010; (b) surface-intensified cyclonic eddy C_4^* observed in June 2011. On the three left-hand side plots, we draw profiles of potential temperature, salinity, and density. The orange lines correspond to the CTD cast carried out within the eddies core, other light gray lines are those from the *far-field* region (i.e., <150 km from the core station collected during the same cruise). The black profile is the mean of all the *far-field* profiles. On the two right-hand side plots, each eddy is represented by colored contours representing temperature and salinity from the *far-field* to the eddies core, as well as isopycnal contours.

[*Crépon et al.*, 1982]. The Burger number quantifies the ratio of the deformation radius to the eddy radius: $Bu \equiv [NH/fR]^2 = [R_d/R]^2$. For each eddy, H is defined as the height over which orbital velocities are greater than $0.2V^{bc}_{\max}$ with V^{bc} the baroclinic orbital velocity rescaled between its minimum and maximum values. When gliders sampled vortices deeper than 1000 m, H was alternatively defined as twice the distance between $0.2V^{bc}_{\max}$ and $V^{bc}_{\max}$ or the maximum sampling depth of 1000 m. In such a case, H is certainly underestimated, as well as the Burger number. Finally, for anticyclonic SCVs observed with R/Vs, H is taken as the vertical extension of their weakly stratified core.

The buoyancy frequency N was computed within (N_{scv}) and outside (N_{out}) each eddy. N_{out} was used to compute the Burger number. The *far-field* region for gliders and mooring data was defined between $2R$ and $4R$. For eddies sampled by R/Vs, the *far-field* was defined by averaging the CTD casts carried out during the same cruise at less than 150 km to get a representative view of the area.

Eventually, we estimated the Ertel's Potential Vorticity (PV) at the core depth for each eddy: $q \equiv -\zeta_a \cdot \nabla\sigma/\rho_0$ where $\zeta_a = \nabla\times\mathbf{v} + f\hat{z}$ is the absolute vorticity. Away from surface and bottom boundaries, this quantity is conservatively advected in the ocean interior, where the fluid is governed by the inviscid Boussinesq equations [*Ertel*, 1942]. In nonfrontal regions (i.e., where lateral density gradients are small), the PV can be written as:

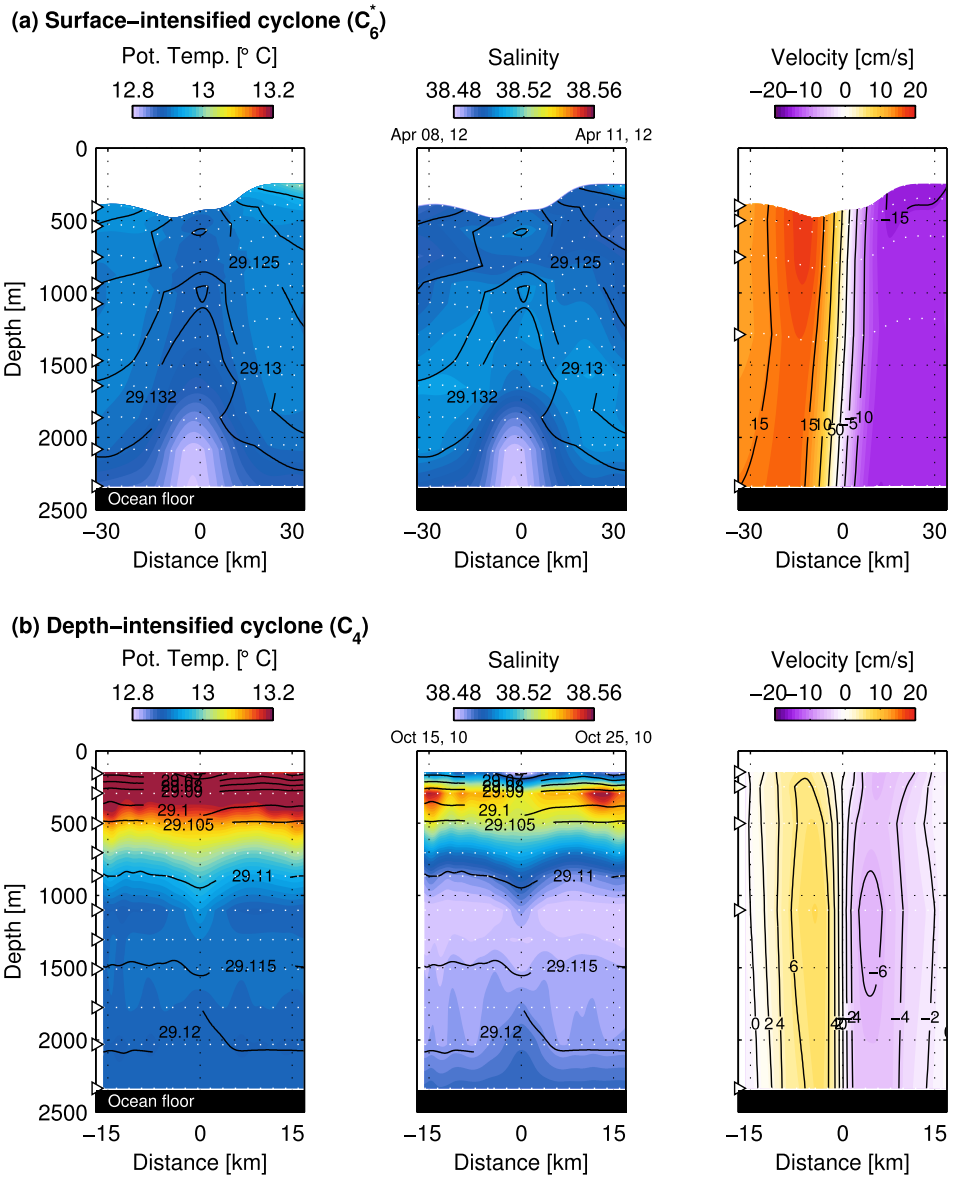

Figure 5. Two cyclonic eddies observed at the LION mooring line: (a) cyclone C_6^* observed in April 2012 exhibiting a core of Shelf Cascading Dense Waters located at the bottom; (b) depth-intensified cyclone C_4 observed in October 2010 with a core located at great depth (>1000 m). For each eddy, the two left plots represent the potential temperature and salinity sections with isopycnals in black. The right plot shows the velocities perpendicular to the mean advection recorded by the current meters. The depth of the sensors is indicated by white triangles and dashed lines. The *x* axis represents the distance along the mean flow advection. Note that this advection is much larger for C_6^* than for C_4, about 20 cm s^{-1} versus 3 cm s^{-1}.

$q = fN^2(1+Ro)/g$. Again, PV was estimated inside ($q_{scv} = fN_{scv}^2(1+Ro)/g$) and outside ($q_{out} = fN_{out}^2/g$) each eddy (see Tables 1 and 2).

2.3.1. Note

The uncertainty in the eddy radii is related to the glider sampling and defined as half the distance between two consecutive glider profiles). Uncertainty in the glider depth-average currents is reasonably considered as 10% of its magnitude [*Merckelbach et al.*, 2008]. The error in *H* is determined by considering the scale over which the eddy signature vanishes in the orbital velocity or hydrography. The error in N_{scv} and N_{out} is defined as the standard deviation of the stratification of close profiles carried out inside and outside each eddy. Finally, the errors indicated in Tables 1 and 2 result from the propagation of those uncertainties through the different formula. As in *Bosse et al.* [2015], *R* and V_{max} are also corrected by a geometric factor (see Appendix A), which is also considered in the error calculation.

AGU Journal of Geophysical Research: Oceans

10.1002/2016JC012144

Table 1. Anticyclonic SCVs Observed in the Northwestern Mediterranean Sea: θ (resp., S) Is the Core Pot. Temperature (resp., Anomaly) Observed Within the SCVs; R the Estimated Radius; V_{max} the Azimutal Peak Velocity; $P@V_{\max}$ the Mean Depth of the Azimutal Peak Velocities; $T_r = 2\pi R/V_{\max}$ the Rotation Period; $Ro = 2V_{\max}/fR$ the Rossby Number; N_{scv} (resp., N_{out}) the Mean Buoyancy Frequency Averaged Over 100 m Within the Core of the SCVs (resp., in the *Far-Field* Region); H an Estimation of the Height of the SCVs; $Bu = [NH/fR]^2$ the Burger Number; q_{scv} (resp., q_{out}) the PV Estimated Within the Core of the SCVs (resp., in the *Far-Field* Region)[a]

Platform	id	Obs.	θ (°C)	S	R (km)	V_{max} (cm s^{-1})	$P@V_{\max}$	T_r (days)	Ro	N_{scv} $\times f$ (s^{-1})	N_{out} $\times f$ (s^{-1})	H (m)	Bu	$q_{scv}/10^{-13}$ (m^{-1} s^{-1})	q_{scv}/q_{out}
Glider	A_1^{wiw}	Feb 2011	12.92	38.40	6.5 ± 1.7	19.6 ± 1.1	150 ± 50	2.4 ± 0.7	-0.61 ± 0.19	10 ± 1	17 ± 1	510 ± 50	1.8 ± 0.7	40 ± 10	0.14 ± 0.06
Glider	A_2^{wiw}	Jun 2012	12.93	38.43	6.5 ± 1.6	17.4 ± 1.1	560 ± 70	2.7 ± 0.8	-0.54 ± 0.16	5.8 ± 1.0	13 ± 1	880 ± 50	2.9 ± 1.1	16 ± 4	0.10 ± 0.04
Glider	A_3^{wiw}	Feb 2013	13.00	38.44	4.1 ± 0.7	18.4 ± 1.2	480 ± 30	1.6 ± 0.4	-0.90 ± 0.21	8.5 ± 0.6	14 ± 1	600 ± 140	4.1 ± 1.7	8 ± 8	0.04 ± 0.04
Glider	A_4^{wiw}	May 2013	13.06	38.41	3.8 ± 0.7	12.4 ± 1.2	100 ± 90	2.2 ± 0.6	-0.68 ± 0.17	20 ± 1	23 ± 1	160 ± 30	0.96 ± 0.35	120 ± 40	0.24 ± 0.10
		Median	12.97	38.42	5.3	17.9	320	2.3	-0.65	9.3	16	560	2.6	28	0.12
		(std)	(0.07)	(0.02)	(1.5)	(3.2)	(230)	(0.5)	(0.16)	(2.0)	(4.5)	(300)	(1.3)	(51)	(0.08)
Glider	A_1^{wdw}	Sep 2012	13.13	38.52	9.3 ± 1.2	15.4 ± 1.1	450 ± 10	4.4 ± 0.9	-0.34 ± 0.07	6.4 ± 0.5	9.6 ± 0.7	>800	$>0.64 \pm 0.14$	25 ± 2	0.30 ± 0.07
R/V	A_2^{wdw}	Sep 2012	13.16	38.53	–	–	~ 500	–	–	6.0 ± 0.7	8.3 ± 1.0	$500 - 1000$	–	–	–
Glider	A_3^{wdw}	Feb 2013	13.18	38.54	4.2 ± 1.3	10.7 ± 1.1	840 ± 160	2.9 ± 1.1	-0.51 ± 0.19	2.6 ± 0.1	3.1 ± 0.1	>640	$>0.22 \pm 0.11$	3.5 ± 0.9	0.36 ± 0.10
Glider	A_4^{wdw}	Jun 2013	13.18	38.54	6.9 ± 0.9	13.0 ± 1.0	670 ± 60	3.8 ± 0.8	-0.38 ± 0.08	2.1 ± 0.1	3.5 ± 0.4	>900	$>0.17 \pm 0.05$	2.7 ± 0.3	0.22 ± 0.03
R/V	A_5^{wdw}	Jun 2013	13.19	38.54	–	–	~ 700	–	–	1.4 ± 0.1	3.6 ± 0.4	$1000 - 1500$	–	–	–
		Median	13.18	38.54	6.9	13.0	670	3.8	-0.38	2.6	3.6	>800	>0.22	3.5	0.30
		(std)	(0.02)	(0.01)	(2.6)	(2.4)	(170)	(0.8)	(0.09)	(2.3)	(3.1)	(230)	(0.26)	(13)	(0.07)
R/V	A_1^{dw}	May 2010	12.95	38.49	–	–	~ 2000	–	–	1.4 ± 0.1	2.7 ± 0.1	~ 2000	–	–	–
Glider	A_2^{dw}	Jan 2011	12.96	38.49	9.1 ± 1.1	$>18.2 \pm 1.0$	>1000	$<3.6 \pm 0.6$	$<-0.41 \pm 0.07$	1.8 ± 0.2	2.6 ± 0.4	>1400	$>0.16 \pm 0.11$	$<1.8 \pm 0.2$	$<0.27 \pm 0.12$
Glider	A_3^{dw}	Jan 2013	13.04	38.51	12.2 ± 1.9	$>6.5 \pm 1.3$	>1000	$<13.7 \pm 4.3$	$<-0.11 \pm 0.03$	0.9 ± 0.2	2.9 ± 0.9	>1700	$>0.16 \pm 0.07$	$<0.57 \pm 0.44$	$<0.08 \pm 0.11$
Glider	A_4^{dw}	Jan 2013	12.93	38.48	7.0 ± 1.4	$>8.0 \pm 1.4$	>1000	$<6.4 \pm 2.0$	$<-0.23 \pm 0.07$	1.9 ± 0.2	2.1 ± 0.2	>1800	$>0.30 \pm 0.10$	$<2.7 \pm 0.4$	$<0.63 \pm 0.23$
Glider	A_5^{dw}	Feb 2013	12.98	38.49	6.0 ± 1.2	$>12.4 \pm 1.7$	>1000	$<3.5 \pm 0.9$	$<-0.42 \pm 0.11$	1.5 ± 0.2	2.9 ± 1.5	>1500	$>0.57 \pm 0.43$	$<1.2 \pm 0.3$	$<0.15 \pm 0.20$
Glider	A_6^{dw}	Feb 2013	12.92	38.48	5.1 ± 1.1	$>11.1 \pm 1.1$	>1000	$<3.3 \pm 1.0$	$<-0.44 \pm 0.13$	1.6 ± 0.6	2.1 ± 1.0	>1600	$>0.42 \pm 0.35$	$<1.4 \pm 0.6$	$<0.34 \pm 0.47$
Glider	A_7^{dw}	Feb 2013	12.95	38.49	14.3 ± 1.7	$>15.0 \pm 1.1$	>1000	$<6.9 \pm 1.3$	$<-0.22 \pm 0.04$	0.8 ± 0.3	2.9 ± 0.7	>1500	$>0.09 \pm 0.05$	$<0.41 \pm 0.48$	$<0.05 \pm 0.09$
Glider	A_8^{dw}	Mar 2013	12.91	38.49	6.4 ± 0.8	$>16.0 \pm 1.1$	>1000	$<2.9 \pm 0.5$	$<-0.51 \pm 0.09$	0.5 ± 0.1	1.8 ± 0.4	>1400	$>0.15 \pm 0.07$	$<0.12 \pm 0.06$	$<0.04 \pm 0.04$
Glider	A_9^{dw}	Jun 2013	12.95	38.49	8.5 ± 1.3	$>6.3 \pm 1.0$	>1000	$<9.9 \pm 3.1$	$<-0.15 \pm 0.05$	3.4 ± 0.1	3.6 ± 0.1	>1500	$>0.40 \pm 0.10$	$<9.6 \pm 0.5$	$<0.75 \pm 0.09$
		Median	12.95	38.49	7.8	>11.8	$1000 - 2000$	<5.0	<-0.32	1.5	2.7	>1500	>0.23	<9.3	<0.21
		(std)	(0.04)	(0.01)	(3.2)	(4.5)	–	(3.9)	(0.15)	(0.8)	(0.5)	(200)	(0.17)	(3.1)	(0.27)

[a]There are dashes where values could not have been estimated due to the observing platform and the SCVs characteristics.

Journal of Geophysical Research: Oceans

10.1002/2016JC012144

Table 2. Cyclonic SCVs Observed in the Northwestern Mediterranean Sea: θ (resp., S) Is the Core Pot. Temperature (resp., Anomaly) Observed Within the SCVs; R the Estimated Radius; V_{max} the Azimutal Peak Velocity; $P@V_{\max}$ the Mean Depth of the Azimutal Peak Velocities; $T_r = 2\pi R/V_{\max}$ the Rotation Period; $Ro = 2V_{\max}/fR$ the Rossby Number; N_{scv} (resp., N_{out}) the Mean Buoyancy Frequency Averaged Over 100 m Within the Core of the SCVs (resp., in the *Far-Field* Region); H an Estimation of the Height of the SCVs; $Bu = [NH/fR]^2$ the Burger Number; q_{scv} (resp., q_{out}) the PV Estimated Within the Core of the SCVs (resp., in the *Far-Field* Region)[a]

Platform	id	obs.	θ (°C)	S	R (km)	V_{max} (cm s^{-1})	$P@V_{\max}$ (m)	T_r (days)	Ro	N_{scv} $\times f$ (s^{-1})	N_{out} $\times f$ (s^{-1})	H (m)	Bu	$q_{scv}/10^{-13}$ (m−1 s^{-1})	q_{scv}/q_{out}
Glider	C_1	May 2010	–	–	8.8 ± 1.3	>14.4 ± 1.0	>1000	<4.5 ± 1.0	>0.33 ± 0.07	1.6 ± 0.2	1.8 ± 0.2	>1700	>0.12 ± 0.04	>3.2 ± 0.6	>1.0 ± 0.4
Glider	C_2	Jun. 2010	–	–	5.6 ± 2.2	5.4 ± 1.4	780 ± 170	7.5 ± 4.1	0.20 ± 0.11	3.4 ± 0.1	3.4 ± 0.2	>1100	>0.44 ± 0.37	13 ± 2	1.2 ± 0.3
Glider	C_3	Jun 2010	–	–	11.7 ± 2.1	>16.7 ± 1.0	>1000	<5.1 ± 1.2	>0.29 ± 0.07	8.2 ± 0.3	4.0 ± 0.1	>1800	>0.38 ± 0.09	>86 ± 6	>5.5 ± 0.6
Mooring	C_4	Oct 2010	12.90	38.48	4.3 ± 0.5	6.1 ± 0.6	1000–1500	5.1 ± 1.2	0.28 ± 0.05	–	–	–	–	–	–
R/V	C_5	Jul 2012	12.87	38.48	–	–	200–400	–	–	22 ± 3	16 ± 4	–	–	–	–
R/V	C_6	Aug 2012	12.86	38.48	–	–	500–700	–	–	7.4 ± 0.6	4.4 ± 0.4	–	–	–	–
Glider	C_7	Sep 2012	–	–	4.1 ± 0.9	>6.3 ± 1.2	>1000	<4.8 ± 1.7	>0.32 ± 0.11	2.4 ± 0.2	2.1 ± 0.2	>1100	0.36 ± 0.28	>6.6 ± 1.1	>1.6 ± 0.6
Glider	C_8	Nov 2012	–	–	3.7 ± 1.3	8.8 ± 1.1	700 ± 10	3.1 ± 1.4	0.49 ± 0.22	7.0 ± 0.5	3.2 ± 0.1	>1200	0.98 ± 0.61	70 ± 21	7.2 ± 2.5
Glider	C_9	Apr 2013	–	–	7.3 ± 1.3	6.3 ± 1.6	490 ± 40	8.5 ± 3.0	0.18 ± 0.06	4.8 ± 0.1	4.4 ± 0.1	940 ± 10	0.32 ± 0.08	26 ± 2	1.4 ± 0.2
Glider	C_{10}	May 2013	–	–	6.4 ± 1.2	9.7 ± 1.1	320 ± 120	4.8 ± 1.3	0.31 ± 0.09	4.4 ± 0.2	4.2 ± 0.2	930 ± 30	0.37 ± 0.10	24 ± 2	1.5 ± 0.3
Glider	C_{11}	May 2013	–	–	5.8 ± 0.6	16.8 ± 1.6	200 ± 10	2.5 ± 0.4	0.62 ± 0.09	10 ± 0.1	5.8 ± 0.3	500 ± 210	0.25 ± 0.15	140 ± 20	5.0 ± 1.2
Glider	C_{12}	May 2013	–	–	7.7 ± 1.1	17.5 ± 1.2	510 ± 10	3.2 ± 0.6	0.47 ± 0.09	4.5 ± 0.1	3.7 ± 0.1	870 ± 40	0.17 ± 0.03	28 ± 3	2.2 ± 0.3
Glider	C_{13}	Jun 2013	–	–	5.3 ± 0.8	8.2 ± 1.0	580 ± 20	4.7 ± 1.3	0.31 ± 0.08	7.5 ± 0.7	4.3 ± 0.1	900 ± 80	0.53 ± 0.13	75 ± 7	3.9 ± 0.6
Glider	C_{14}	Oct 2013	–	–	7.3 ± 1.2	11.9 ± 1.0	720 ± 20	4.4 ± 1.1	0.35 ± 0.09	9.4 ± 0.2	6.7 ± 0.1	>1000	>0.88 ± 0.61	100 ± 10	2.7 ± 0.3
		Median	12.87	38.48	6.1	8.8	600	4.8	0.32	7.0	4.1	500–1800	0.37	28	2.2
		(std)	(0.02)	–	(2.3)	(4.6)	(300)	(1.7)	(0.12)	(5.2)	(3.3)	–	(0.27)	(45)	(2.1)
Glider	C_1^*	Mar 2011	–	–	8.0 ± 0.8	12.2 ± 1.1	Surface	4.7 ± 0.8	0.31 ± 0.06	11 ± 1	18 ± 6	170 ± 40	0.14 ± 0.09	150 ± 10	0.52 ± 0.40
Glider	C_2^*	Mar 2011	–	–	6.2 ± 1.4	11.8 ± 1	Surface	3.9 ± 1.2	0.39 ± 0.12	19 ± 2	31 ± 13	70 ± 30	0.11 ± 0.12	480 ± 70	0.53 ± 0.53
Glider	C_3^*	Apr 2011	–	–	7.3 ± 1.9	16.1 ± 1.1	Surface	3.3 ± 1.0	0.45 ± 0.14	22 ± 3	36 ± 7	170 ± 40	0.69 ± 0.40	700 ± 120	0.57 ± 0.34
R/V	C_4^*	Jun 2011	12.91	38.48	–	–	0–300	–	–	34 ± 6	30 ± 5	–	–	–	–
Glider	C_5^*	Apr 2012	–	–	12.0 ± 1.7	14.7 ± 1.0	Surface	5.9 ± 1.2	0.25 ± 0.05	32 ± 5	37 ± 15	320 ± 70	1.0 ± 0.7	1300 ± 100	0.94 ± 0.83
Mooring	C_6^*	Apr 2012	12.82	38.47	12.2 ± 2.1	16.3 ± 0.6	0–400	5.5 ± 1.2	0.27 ± 0.06	–	–	–	–	–	–
Glider	C_7^*	Mar 2013	–	–	9.9 ± 1.2	19.9 ± 1.1	Surface	3.6 ± 0.6	0.40 ± 0.07	1.6 ± 0.2	20 ± 1	180 ± 50	0.13 ± 0.06	3.5 ± 0.7	0.009 ± 0.002
Glider	C_8^*	Mar 2013	–	–	6.8 ± 2.0	24.7 ± 2.4	50 ± 40	2.0 ± 0.6	0.76 ± 0.23	34 ± 1	25 ± 3	250 ± 60	0.88 ± 0.56	1800 ± 100	3.1 ± 2.4
R/V	C_9^*	Apr 2013	12.92	38.49	–	–	0–200	–	–	19 ± 1	17 ± 1	–	–	–	–
Glider	C_{10}^*	Apr 2013	–	–	7.5 ± 1.7	17.3 ± 2.2	30 ± 10	3.2 ± 0.8	0.46 ± 0.12	26 ± 3	28 ± 1	240 ± 70	0.81 ± 0.43	1000 ± 200	1.3 ± 0.3
Glider	C_{11}^*	May 2013	–	–	10.3 ± 1.0	15.3 ± 1.0	Surface	4.9 ± 0.8	0.31 ± 0.05	63 ± 7	67 ± 13	190 ± 30	1.6 ± 0.6	4700 ± 300	1.1 ± 0.5
		Median	12.91	38.48	8.0	16.1	0–100	3.9	0.39	24	29	190	0.75	850	0.76
		(std)	(0.06)	(0.01)	(2.2)	(4.0)	–	(1.2)	(0.15)	(17)	(15)	(70)	(0.52)	(1500)	(0.94)

[a]There are dashes where values could not have been estimated due to the observing platform and the SCVs characteristics.

3. Results

3.1. Basin-Scale Context

For the whole study period (November 2009–October 2013), the LION mooring combined with other observing platforms (Argo floats, gliders, and R/Vs) provide insightful information about open-ocean deep convection that can occur in the Gulf of Lions in winter. The region affected by the deepest vertical mixing is usually centered around 42°N–5°E (see Figure 1). In that area, the temperature and salinity profiles collected show a mixed layer reaching the bottom of the ocean (between 2300 and 2500 m) around mid-February every year from 2010 to 2013 (Figure 6a).

The eastern part of the basin (i.e., the Ligurian Sea) is generally an area of intermediate to deep mixing (200–1000 m) subjected to an important year-to-year variability [*Marty and Chiavérini*, 2010]. In the absence of a highly instrumented mooring line like in the Gulf of Lions, the sampling of the Ligurian Sea is sparser. However, especially thanks to autonomous platforms (gliders and profiling floats), the temporal evolution of the water column can still be described (see Figure 6b). During all winters from 2010 to 2013, in situ observations did not reveal any sign of mixing deeper than 1000 m. In 2010 and 2011, winter mixing seems not to be deeper than 400 m, while it reached 700–1000 m in 2012 and 2013. In particular, the winter 2013 is characterized by a mixed layer depth of ∼1000 m, which has been repetitively observed in the Ligurian Sea by both shipborne CTD casts and a glider in February during an intense observing period. By that time, the mixed patch was quite warm and salty $\theta \simeq 13.18^{\circ}$C and $S \simeq 38.54$ (like in 2012) compared to winters of shallower mixing. This is mainly because if it exceeds the depth of the warm and salty Levantine Intermediate Waters (LIW) located around 300–500 m, the heat and salt contents of the mixed layer increase.

Finally, it is worth mentioning that the deep waters production can also occur on the shelf of the Gulf of Lions. This phenomenon takes place less often than open-ocean deep convection in the NW Mediterranean Sea. The recent major events of shelf dense waters cascading are the winters 2005, 2006 [*Puig et al*., 2013], and 2012 [*Durrieu de Madron et al*., 2013]. The latter study describes the story line of the 2012 event. In February, mooring lines deployed on the continental slope of the Gulf of Lions observed an intense cascading event of dense waters. In April, the signature of a dense bottom water mass—fresher and colder than the deep waters formed by open-ocean deep convection—was observed at the LION mooring, propagating toward the abyssal plain. Then in July, the MOOSE-GE cruise showed the spreading of these new Shelf Cascading Dense Waters (SCDW) over the whole basin surface.

During the whole study period, the wintertime deep convection in the NW Mediterranean Sea can be considered as a consistent process from 1 year to another. The mixing always reached the bottom in the Gulf of Lions and an intermediate depth in the Ligurian Sea (300–1000 m) and the newly formed waters present each year similar characteristics (colder/fresher at intermediate depths, warmer/saltier at great depths) with respect to the background.

3.2. Eddies Characterization and Classification

3.2.1. Anticyclonic Eddies

All anticyclonic eddies in this study are characterized by a weakly stratified core of nearly homogeneous waters with horizontal extent on the order of the internal Rossby radius or less (see Figures 3a and 4a), similar to "Submesoscale Coherent Vortices" (SCVs) first described by *McWilliams* [1985]. The dynamical adjustment of a convected water parcel intruded into a stratified environment has been studied as a possible generation mechanism [*McWilliams*, 1988]. Anticyclonic SCVs can thus be formed at depths varying with depth of the mixed layer impacting the hydrographical characteristics of their core, as shown in the θ/S diagram of Figure 2. The 18 anticyclonic SCVs were hence classified into three categories depending on the water mass of their core.

Winter Intermediate Waters (WIW): SCVs A_i^{wiw} with $i \in [1,4]$ in Table 1 have a relatively cold ($12.97 \pm 0.07^{\circ}$C) and fresh (38.42 ± 0.02) core located in the upper layers between 0 and 300 m (see an example in Figure 3a). This water mass results from the shallow vertical mixing of fresh modified Atlantic Waters (AW) under the action of strong air/sea interactions. This water mass is classically called Winter Intermediate Waters. They can be formed early during winter in the central part of the Gulf of Lions, then later on around the deep convection zone and in the Ligurian Sea, where meteorological conditions are

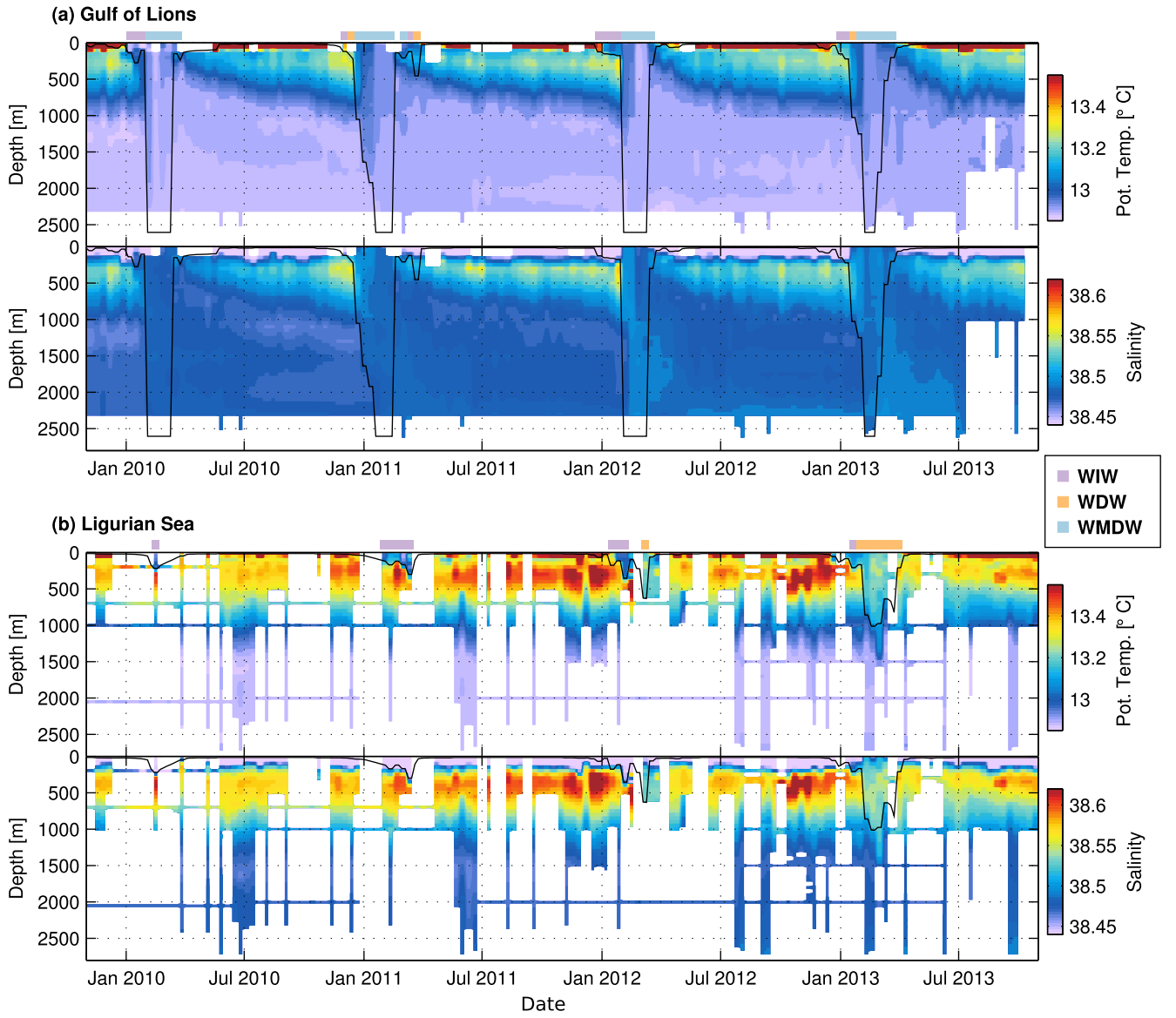

Figure 6. (a) Upper plot: Temporal evolution of potential temperature and salinity in the "Gulf of Lions" (as defined in Figure 1). All available in situ observations collected by R/Vs, gliders, Argo floats, and mooring lines have been averaged within 10 days intervals and vertical layers of 50 m. The black line represents the evolution of the mixed layer depth computed on temperature with a 0.1°C criterion (i.e., it corresponds to the depth where $|\theta - \theta_{ref}| > 0.1$°C with θ_{ref} the potential temperature of the first 0–50 m layer). The winter mixed layer is associated with a water mass regarding its θ/S characteristics (see colors above the plots): $S < 38.46$ for WIW, $\theta > 13.05^{\circ}$C for WDW, and $\theta < 13.05^{\circ}$C for WMDW. Those delimitations are drawn in Figure 2. (b) Same but in the "Ligurian Sea" (as defined in Figure 1).

less severe and the mixing often restricted to the upper layers [*Millot*, 1999]. The WIW can also be formed on the continental shelves of the Gulf of Lions and the Balearic Sea [*Vargas-Yáñez et al.*, 2012; *Juza et al.*, 2013].

Winter Deep Waters (WDW): SCVs A_i^{wdw} with $i \in [1, 5]$ in Table 1 have a quite warm ($13.18 \pm 0.02^{\circ}$C) and salty (38.54 ± 0.01) core located slightly deeper between 500 and 1000 m below the depth of the warm and salty LIW (see for example Figure 3b). When the vertical mixing partly or totally incorporates the LIW layer, the mixed layer gets warmer and saltier, as observed with the core characteristics of SCVs A_i^{wdw} compared to A_i^{wiw}. On a θ/S diagram, this water mass lies on the mixing line between the LIW and the WMDW (see Figure 2). Note that the name "Winter Deep Waters" has never been mentioned in the literature before to our knowledge. This study shows the importance of defining a distinct water mass resulting from the intermediate mixing of AW and LIW. From the various eddies observed, this new classification of the water

masses appears to be necessary to characterize periods and areas of strong intermediate mixing that stops just above the WMDW levels (≃500–1000 m).

Western Mediterranean Deep Waters (WMDW): SCVs A_i^{dw} with $i \in [1,9]$ in Table 1 have core characteristics ($\theta \sim 12.95 \pm 0.04^{\circ}$C and $S \sim 38.49 \pm 0.01$) close to the Western Mediterranean Deep Waters (WMDW) (see Figure 2). They are characterized by a positive θ/S anomaly compared to the surrounding deep waters of about +0.05°C and +0.01 (see Figures 2 and 4a). They result from deeper mixed layers (>1000 m) than the first two categories. For those mixed layer depths, the mixing involves the surface and intermediate layers of AW and LIW, as well as a significant part of the preexistent deep waters.

Note that gliders are not able to reach the core depth of WMDW anticyclones, because of their maximal diving depth of 1000 m (see Figure 3a). Only by examining the glider-derived density sections, one cannot discriminate their deep isopycnals doming from that of a cyclonic eddy. Their identification as depth-intensified anticyclones was then possible thanks to the depth-average currents estimated by the gliders showing their sense of rotation. In this particular case, depth-average currents were of crucial importance.

3.2.2. Cyclonic Eddies

The cyclonic eddies are all characterized by a doming of the dense isopycnals extending from the bottom sometimes up to the surface layers (see Figure 3b). Between the *far-field* and the eddies core, isopycnals can be raised up by about 1000–1500 m at great depth. We identify the core of a cyclonic SCV as the weakly stratified part of the water column embedded within the described isopycnals doming. As for anticyclonic SCVs, this core is characterized by nearly homogeneous waters, but it is trapped at the bottom of the ocean (see Figure 4b). Identification of the core θ/S characteristics could not be reliably carried out when cyclonic SCVs were sampled by gliders, but shipborne CTD casts and the LION mooring line could fill this gap (see Table 2).

Regarding the core characteristics of cyclonic eddies, they are generally typical of WMDW ($\theta \sim 12.90^{\circ}$C and $S \sim 38.49$). As it can be observed on the θ/S diagram of Figure 2, they are all denser (fresher, but colder) than anticyclonic SCVs of WMDW. Interesting examples (C_5, C_6, and C_6^* in Table 2) are found to have core characteristics significantly fresher and colder than usual WMDW with a potential temperature ranging 12.82–12.87°C and a salinity of 38.47–38.48 (see Table 2). This kind of signal in the deep water masses has been clearly identified as resulting from winter dense waters production on the shelf of the Gulf of Lions [*Béthoux et al*., 2002]. Those waters can then cascade and spread out over the abyssal plain. These particular eddies were coherently all observed in 2012 after the occurrence of a major episode of cascading [*Durrieu de Madron et al*., 2013], while such phenomenon was possibly less intense the other years. The cascading of shelf dense waters seems thus possible mechanism of generating coherent cyclonic structures if they are dense enough to reach the bottom of the deep basin, as in 2012.

When cyclones extend to the surface, the warm and salty signature of LIW is importantly attenuated in their core (see Figures 3b and 4b). By the time of their formation, these eddies should thus have been in contact with eroded LIW, typical of the western part of the basin, and potentially vertically mixed. Dynamical barriers set by the eddy rotation then certainly inhibited the lateral diffusion of the surrounding warm and salty LIW toward the eddies core.

In total, 25 cyclonic eddies have been identified for the study period. They were classified into two categories based upon dynamical considerations rather than on hydrographical ones. All cyclones are indeed found to have a similar hydrographical signature with a weakly stratified core at great depth. In contrast, their dynamical signature was different either characterized by: (1) depth-intensified velocities, a peculiar isopycnals pinching at depth and a small radius (C_i with $i \in [1,14]$ in Table 2); or (2) surface-intensified velocities, an isopycnals doming extending to the surface and a greater radius (C_i^* with $i \in [1,11]$ in Table 2). This is a noticeable difference with the anticyclonic SCVs whose orbital velocities peak at the depth of their weakly stratified core.

3.3. Origin

3.3.1. Anticyclonic Eddies

Figure 6 shows the mixed layer depth and its θ/S characteristics in two key regions of the NW Mediterranean Sea: the Gulf of Lions and the Ligurian Sea (Figure 1). The mixed layer is further classified in terms of water mass, as explained in the legend of Figure 6. WIW are detected in the Gulf of Lions and in the Ligurian Sea at the early stage of winter mixing, when the mixed layer depth does not exceed about 300 m. WDW

are formed in 2012 and 2013 only in the Ligurian Sea, when the mixed layer depth reached 500–1000 m. In the Gulf of Lions, the mixing reached the bottom each year of the study period. WDW are identified there, but only for a short period of time while the mixed layer is deepening. This water mass is then rapidly transformed into newly formed WMDW, the ultimate product of winter mixing that can be produced in the center of the preconditioning cyclonic gyre around 42°N, 5°E.

Convective regions are already known as a potential source for the generation of subsurface anticyclonic SCVs [*McWilliams*, 1985]. The mixed layer classification enables the identification of the region and timing associated with the generation of the observed anticyclones regarding the water mass composing their cores (see Table 1). WIW SCVs should thus be preferentially formed in areas of shallow mixing. This could be the Ligurian Sea, as already reported by *Gasparini et al.* [1999], where the mixing is usually less pronounced as in 2010 and 2011 for instance. Some WIW anticyclones were, however, also observed in 2012 and 2013. These years, WDW was formed in the Ligurian Sea as the mixing reached deeper levels. It indicates such they could also be formed in the early stage of winter mixing throughout the whole basin before being shed out of the mixing zone. Anticyclonic vortices characterized by WDW cores were only observed in 2012 and 2013, which coincides with WDW formation observed in the Ligurian Sea (see Figure 6b). The observed WDW anticyclones were thus very likely generated in this area during winters 2012 and 2013. Finally, WMDW anticyclones could only be formed in areas of deeper mixing exceeding 1000 m, but certainly before the mixing reached the bottom.

Other generation mechanisms exist for anticyclonic SCVs like the instability of a coastal undercurrent [*D'Asaro*, 1988b; *Molemaker et al.*, 2015] or the interaction of large-scale eddies with the topography [*Vic et al.*, 2015]. In the NW Mediterranean Sea, the first mechanism has been identified to be important along the northwestern part of Sardinia leading to the formation of "Suddies" characterized by warm and salty LIW [*Bosse et al.*, 2015]. In this study, those processes are however not relevant as the θ/S characteristics of the observed anticyclonic SCVs differ from the boundary circulation at similar depth.

3.3.2. Cyclonic Eddies

Cyclonic eddies are all associated with a deep isopycnal doming, which caps a bottom-trapped weakly stratified core of WMDW or SCDW (see Figures 4b and 5). It is known that the rim-current circling the mixed patch of a deep convection area generally becomes baroclinically unstable because of the strong potential energy increase of the system induced by vertical mixing [*Gascard and Clarke*, 1983]. Instability meanders can hence intrude homogeneous fluid parcel into the stratified surrounding environment. In order to form cyclonic eddies with a bottom core of newly formed deep waters, the equilibrium depth of those intrusions has to correspond to the seafloor. Their generation therefore most likely occurs after the mixed layer reaches the bottom, as was observed in the Gulf of Lions for the study period (Figure 6a). A numerical modeling study of the NW Mediterranean Sea consistently described the genesis of deep waters cyclones [*Damien*, 2015].

Furthermore, tank experiment and numerical studies of rotating Rayleigh-Bénard convection revealed a transition, as the influence of rotation increases, from rapidly evolving convection rolls to the presence of more persistent cyclonic structures [*Bubnov and Golitsyn*, 1985; *Zhong et al.*, 1991; *Julien et al.*, 1996]. In the ocean, the Earth's rotation becomes important for mixed layers exceeding a critical depth: $H^* = \sqrt{B_0/f^3}$ with *Bo* the buoyancy loss due to air-sea exchanges [*Marshall and Schott*, 1999]. For typical conditions of the NW Mediterranean Sea ($B_0 = 5\ 10^{-7}$ m^2 s^{-3}), the observed mixed layer depth ($>$2000 m) is much larger than H^* ($\simeq$ 700 m). Hence, rotation plays an important role in winter convection that can promote the formation of cyclonic vortices.

3.4. Dynamical Characteristics

3.4.1. Anticyclonic SCVs

Anticyclonic SCVs have peak velocities located well below the pycnocline and depending on their core water mass: 320 $\pm$ 230 m for A_i^{wiw}, 670 $\pm$ 170 m for A_i^{wdw}, and $>$1000 m for A_i^{dw}. The only example of anticyclonic SCV sampled by full-depth shipborne CTD casts shows flat isopycnals near 2000 m indicating the approximate position of the velocity maximum and a height *H* of nearly 2000 m (see Figure 4a).

Their peak velocities are intense: 17.9 $\pm$ 3.2 cm s^{-1} for A_i^{wiw}, 13.0 $\pm$ 2.4 cm s^{-1} for A_i^{wdw}, and $>$11.8$\pm$ 4.5 cm s^{-1} for A_i^{dw}. Due to their slightly smaller radii and stronger velocities, WIW SCVs observed close to the surface have greater Rossby numbers compared to deeper SCVs: -0.65 ± 0.16 for A_i^{wiw}, -0.38 ± 0.09 for A_i^{wdw}, and $>-0.32\pm0.15$ for A_i^{dw} (see Figure 7a and Table 1). V_{max} and *Ro* are, however, underestimated for deep

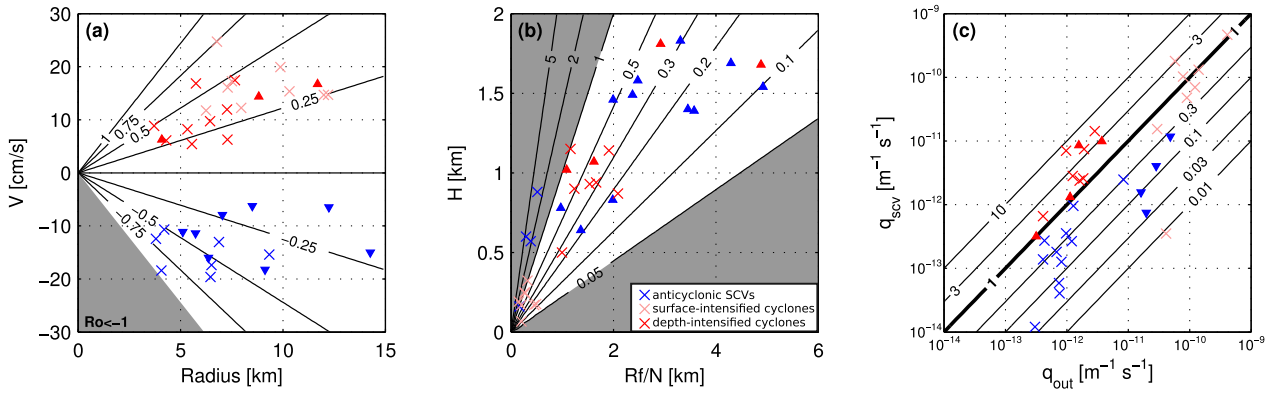

Figure 7. (a) $V_{max}=f(R)$ with lines corresponding to the Rossby number; (b) $H=f(Rf/N_{out})$ with lines corresponding to the Burger number; (c) $\log(q_{scv})=f(\log(q_{out}))$ with lines corresponding to the ratio q_{scv}/q_{out}. Anticyclones are represented in blue and cyclones in red. Surface-intensified cyclones (in light red) have been distinguished from depth-intensified ones (deep red), because of their clearly different vertical extension and effect on the PV field. When the value of V_{max} or H corresponds to an underestimation (resp., overestimation), we mark it with a triangle oriented to the bottom (resp., to the top) of the figure.

WMDW SCVs because glider sampling is restricted to the upper 1000 m. Those numbers are consistent with *Testor and Gascard* [2006] reporting Rossby numbers of about −0.5 for similar anticyclonic SCVs of newly formed deep waters. Therefore, those subsurface anticyclones can be considered as nonlinear submesoscale flows. This is especially true for A_i^{wiw}, which are almost inertially unstable, i.e., $Ro < -1$ for barotropic vortices [*Kloosterziel et al.*, 2007; *Lazar et al.*, 2013]. High nonlinearity also implies strong resistance regarding the interaction with larger scale balanced flows [*McWilliams*, 1985]. Moreover, those large-scale currents are generally weaker at depth and are characterized by a reduced shear and strain. This might help deep SCVs to survive for long periods of time.

The radius of anticyclonic SCVs increases with depth: WIW SCVs have a radius of 5.3 ± 1.5 km, WDW SCVs of 6.9 ± 2.6 km and SCVs of deep waters of 7.8 ± 3.2 km (Table 1). As previously mentioned, the ratio of their radius to the deformation radius defines the Burger number: $Bu \equiv [R_d/R]^2$. *McWilliams* [1985] reported stability bounds for SCVs: $0.05 < Bu < 1$. Similarly, *Carpenter and Timmermans* [2012] computed the aspect ratio (H/R) of a density perturbation introduced into uniformly stratified waters and found: $Bu=[\ln(10)/\pi]^2 \simeq 1$. These numerical and theoretical considerations are consistent with observational studies made at various places of the world's ocean describing SCVs [*D'Asaro*, 1988a; *Timmermans et al.*, 2008; *Bower et al.*, 2013; *Pelland et al.*, 2013; *Bosse et al.*, 2015]. The large aspect ratio close of deep anticyclonic SCVs can thus be explained by those constraints on the Burger number and the low stratification of the deep basin. The stability interval is fairly respected for A_i^{wdw} and A_i^{dw} (see triangles in Figure 7b). The SCVs A_i^{wiw} have, however, greater Burger numbers of 2.6 ± 1.3 (crosses in Figure 7b). These eddies could be less stable and have to adjust their aspect ratio to gain stability [*Griffiths and Linden*, 1981]. Note that the analysis of *Carpenter and Timmermans* [2012] assumes a constant stratification, which is less valid at depths WIW anticyclones were observed.

All anticyclonic SCVs have a weakly stratified core compared to the far-field: $N_{scv} < N_{out}$ (see Table 1). On average, the core stratification is reduced by about 30–40%. Combined with their strong negative vorticity, they also represent local minima of the potential vorticity with a reduction of 70–90% (see Figure 7c). This PV reduction is about double that associated with anticyclonic SCVs of Levantine Intermediate Waters described in *Bosse et al.* [2015]. This difference might be related to their different generation mechanism. The latter SCVs are indeed generated by the interaction of an undercurrent with the continental slope [*D'Asaro*, 1988b]. Vertical mixing caused by air-sea fluxes seems much more effective in destroying PV than bottom friction, as it drastically reduces the water stratification to almost zero.

3.4.2. Cyclonic Vortices

As stated in section 3.2.2, cyclonic vortices have been classified into two categories: surface-intensified eddies (C_i^*) characterized by peak velocities within the upper 100 m (see Figures 3b1 and 5a), and depth-intensified eddies (C_i) having peak velocities well below the thermocline at ≃600 ± 300 m depth (see Figures 3b2 and 5b). Compared to surface-intensified cyclones, subsurface cyclonic eddies are characterized by smaller radii (6.1 ± 2.3 km versus 8.0 ± 2.2 km), but less intense velocities (8.8 ± 4.6 cm s^{-1} versus 16.1 ± 4.0 cm s^{-1}). This yields similar high Rossby numbers for both categories +0.32± 0.12 for C_i

and $+0.39\pm 0.15$ for C_i^* (see Figure 7a and Table 2). These numbers are in good agreement with the previous study of *Testor and Gascard* [2006] describing submesoscale cyclonic eddies escaping the deep water formation zone.

It worth mentioning that surface-intensified cyclones have a important barotropic component. For those eddies, the orbital velocities observed near 1000 m depth represent on average ~40% of their peak velocities (see Figures 3b and 5a). After the winter mixing phase, currents measurements at the mooring LION show very intense barotropic currents in the Gulf of Lions (up to 40 cm s^{-1} over the whole water column) (Houpert et al., submitted manuscript). The barotropic structure of cyclones C_i^* could thus be remnant of the deep convection restratification phase. Those eddies significantly contribute to the deep waters dynamics. Their structure is very similar to cones of convected waters described in laboratory [*Maxworthy and Narimousa*, 1994] and numerical modeling [*Jones and Marshall*, 1993; *Send and Marshall*, 1995]. In particular, *Maxworthy and Narimousa* [1994] predicted the radius of these structures: $5h\sqrt{Ro^*}$, where $Ro^* \equiv [B_0/f^3h^2]^{1/2}$ is an adimensional number relevant for convective sites characterized by buoyancy loss *Bo* and a water depth *h*. Choosing parameters suited to the NW Mediterranean Sea ($B_0 = 5\,10^{-7}$ m^2 s^{-3}, $h = 2500$ m) yields a radius of the convected cones of about 7 km, which is very similar to the observed median radius of 8.0 ± 2.2 km (see Table 2).

Cyclonic vortices are characterized by weakly stratified deep waters (see Figure 4b). This hydrographical core extends from the bottom to intermediate depths for C_i, and near the pycnocline for C_i^*. As weakly stratified waters are brought close to the surface, surface-intensified cyclones are generally characterized by a weaker stratification compared to the *far-field* (see Figure 8b). In contrast, depth-intensified vortices C_i exhibit a local stratification increase at the depth of their peak velocities (see Figures 5b and 8c). Subsurface cyclones tend to have a much larger vertical extension than surface-intensified cyclones: $H > 1000$ m for C_i versus 190 ± 70 m for C_i^* (see Figure 7b). Due to difference in their background stratification, both categories have nonetheless similar Burger numbers: 0.37 ± 0.27 for C_i and 0.75 ± 0.52 for C_i^*. These numbers are comparable to anticyclonic SCVs.

Surface-intensified cyclones C_i^* do not systematically imply a local maximum of the PV field. The weak stratification observed close to their velocity maximum compensate the effect of the cyclonic vorticity on the PV. Their overall effect on the PV field is thus variable from one eddy to the other (see Figure 7c and Table 2). On the other hand, depth-intensified cyclones C_i have a local stratification increase of about 70%: $N_{scv} = 7.0 \pm 5.2f$ versus $N_{out} = 4.1 \pm 3.3f$. Combined with a strong cyclonic vorticity, this importantly enhances the PV field: $q_{scv}/q_{out} \sim 2.2$ (see Figure 7c and Table 2).

3.5. Deep Convection Preconditioning

Both anticyclonic and cyclonic vortices impact the water column stratification, thus further modifying its buoyancy content. These eddies are observed here throughout the whole year and it is already known that SCVs can persist for more than a year [*Armi et al.*, 1988; *Ronski and Budéus*, 2006; *Testor and Gascard*, 2006]. Hence, they could impact affect the convective event of the winter following their generation, as previously considered from in situ observations [*Lherminier et al.*, 1999] and numerical modeling [*Legg et al.*, 1998].

In order to discuss the eddy influence on the mixed layer deepening, we define $\Gamma(z)$ the mixed layer deepening ratio (see Appendix B): when $\Gamma > 1$ (resp., $\Gamma < 1$) the mixed layer will deepen faster (resp., slower) by a factor of Γ within the eddy compared to the background. Note that this quantity is only based on the water column buoyancy content $IS(z)$ ($= \int_{z_0}^{z} N^2(z\prime)z\prime \mathrm{d}z\prime$, more details in Appendix B) and does not take into account any horizontal effect.

Because gliders only sample the upper part of deep vortices, the different types of eddies were examined using full-depth shipborne CTD casts carried out during the MOOSE-GE summer cruises (see Figure 8). The buoyancy content was computed with a reference depth z_0 greater than 250 m depth to remove the effect of the surface layers having a highly variable buoyancy content over space and time due to a high variability of the seasonal thermocline intensity and depth. At depth, the water column buoyancy content is significantly influenced by deep eddies resulting in important effect on the vertical mixing.

3.5.1. Anticyclonic SCVs

The weakly stratified core of anticyclonic SCVs facilitates its vertical mixing. For instance, a clear decrease of the vertical stratification for SCV A_1^{dw} between about 1200 and 2500 m can be noticed (see Figure 8a, middle

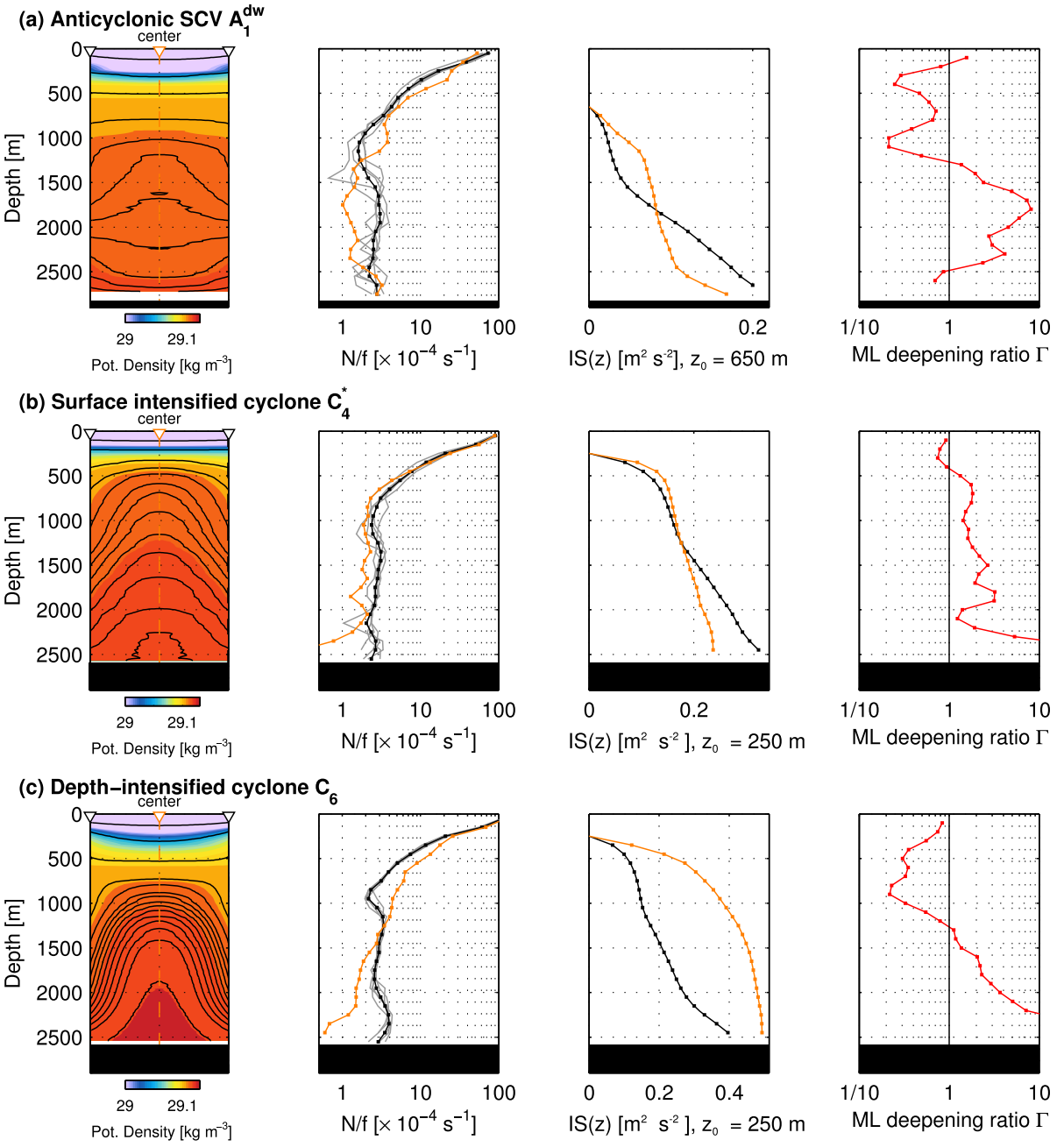

Figure 8. For (a) anticyclone A_1^{dw}, (b) surface-intensified cyclone C_4^*, and (c) depth-intensified cyclone C_6 sampled by R/Vs, we represent: (left) their density section from the *far-field* to the core; (middle left) the stratification normalized by the Coriolis parameter *f* for the *far-field* profiles in light gray, their mean in black and for the eddy core in orange; (middle right) the columnar buoyancy with depth integrated from a reference depth (650 m for (a) and 250 m for (b) and (c)) within the eddy in orange and in the *far-field* in black; (right) the mixed layer deepening ratio between the *far-field* and the eddy core. Note that the *x* axis is logarithmic for the middle left and the right plot.

left). This large core is associated with a mixed layer deepening ratio Γ greater than unity. On average, the mixed layer will then deepen about four times faster in the SCV's core than outside. In contrast, the stratification is enhanced below and above this core. For SCV A_1^{dw}, Γ peaks at almost 1/5 above the core above 1000 m depth. The overall effect of the SCV on the columnar buoyancy from the top of the SCV at 650 m to the bottom corresponds to a global reduction of about 0.06 m^2 s^{-2} (∼30% of the background buoyancy content). This quantity is roughly the buoyancy loss caused by a few days winter storm.

It is worth mentioning that surface and subsurface eddies can interact. For example, SCV A_1^{dw} is observed at the same location of a surface WIW anticyclone, which has a clear signature at 100–200 m depth (see

Figure 4a). The columnar buoyancy is also influenced by this surface eddy: considering $z_0 = 0$ m, IS(700 m) = 0.65 $m^2\ s^{-2}$ within the eddy core and 0.49 $m^2\ s^{-2}$ outside. This important increase of 0.16 $m^2\ s^{-2}$ (+30%) illustrates the important role of surface mesoscale eddies in the initiation of the mixing during fall and early winter.

3.5.2. Surface-Intensified Cyclones

They are characterized by isopycnal doming extending up to the surface (see Figure 8b), which favors vertical mixing over the whole water column, once the seasonal thermocline has been mixed. For cyclone C_4^*, the mixed layer deepening ratio is coherently found to be always greater than one from below the seasonal thermocline to the bottom. The mixed layer deepening will then be twice faster within the eddy core than around it for a same buoyancy loss. The total buoyancy flux reduction due to this cyclone reaches about 0.09 $m^2\ s^{-2}$, which is significantly larger than the reduction associated with the anticyclonic SCV A_1^{dw}. Surface-intensified cyclone might thus have an important effect on the vertical mixing.

3.5.3. Depth-Intensified Cyclones

Those cyclones have a peculiar density structure characterized by an isopycnal pinching at the depth of their peak velocities. The stratification is then locally increased compared to the far-field, creating a barrier to vertical mixing. For instance, Γ reaches $\simeq$1/4 between the upper levels and 1200 m for the cyclone C_6 (see Figure 8c) and represent a cumulated columnar buoyancy increase of 0.1–0.2 $m^2\ s^{-2}$. Nevertheless, below this local stratification increase, the water column remains quite homogeneous and less stratified than surrounding waters favoring the mixed layer deepening down to the bottom: $\Gamma > 1$ below about 1200 m. The overall effect of the depth-intensified cyclone C_6 is though an increase of the integrated columnar buoyancy. Due to their particular density structure, depth-intensified cyclones seem to be barriers for the vertical mixing.

The above examples demonstrate how complex is the water column preconditioning for vertical mixing by (sub)mesoscale eddies. Only surface-intensified cyclones correspond to a reduction of the whole water column buoyancy content below the surface layer. Two contrasted cases are found for depth-intensified eddies: anticyclonic SCVs favor the mixed layer deepening only through their weakly stratified core, whereas cyclones inhibit it at the depth of their peak velocity. The induced perturbation of the columnar buoyancy is though significant, being comparable or larger than the buoyancy loss of a winter storm (0.05 $m^2\ s^{-2}$). Over the time scale of a typical storm (2–3 days), eddies can therefore strongly enhance/inhibit the mixed layer deepening resulting in differences of several hundreds of meters given the small of the deep levels.

4. Discussion

4.1. A New Concept of Cyclonic SCV

Anticyclones SCVs are known to be able to wander in the ocean interior with lifetime of months to years [*Armi et al*., 1988; *Testor and Gascard*, 2003; *Ronski and Budéus*, 2006; *Bower et al*., 2013; *Søiland and Rossby*, 2013]. In contrast, the literature does not mention the observation of similar long-lived cyclonic coherent structures. *Testor and Gascard* [2006] described postconvective cyclones with RAFOS isobaric Lagrangian floats in the NW Mediterranean, but they could not be observed for more than 2 months. Deep cyclones have also been observed in the Mediterranean outflow [*Carton et al*., 2002], in the Gulf Stream [*Savidge and Bane*, 1999; *Andres et al*., 2015], or in the Denmark strait overflow with a lifetime ranging from weeks to 1–2 months [*Spall and Price*, 1998]. An important characteristic of depth-intensified cyclones described in the present study is their coherence compared to surface-intensified structures. About one-third of them have been observed 6 months or more after the deep convection event (namely February) and up to several hundreds of kilometers far from the deep convection zone, where they are certainly formed, in agreement with a recent regional modeling study [*Damien*, 2015]. This demonstrates depth-intensified cyclones can have an extended lifetime like anticyclonic SCVs. It is although premature to conclude this is a general and common feature of those vortices.

There is a duality between depth-intensified cyclones and anticyclonic SCVs. Both of them can have an extended lifetime with orbital velocities intensified at great depths. Anticyclonic SCVs (resp., depth-intensified cyclones) are local minima (resp., maxima) of potential vorticity due to the weak (resp., strong) stratification and anticyclonic (resp., cyclonic) vorticity found at the depth of peak velocity. Cylones here qualified as "depth-intensified" could therefore be considered as cyclonic SCVs.

4.2. Census of Eddies Formed by Deep Mixing

During the 4 years of the study period, 18 anticyclones and 25 cyclones associated with deep convection were detected with gliders, R/Vs, and the LION mooring line. Of course, there were many more vortices that were not detected and the purpose of this section is to statistically estimate their total number. This is an important issue because those vortices are very efficient at transporting physical, geochemical, and biological tracers over long distances and are thus crucial for the spreading of the intermediate and deep water masses, as well as for the ocean ventilation. In the NW Mediterranean Sea, *Testor and Gascard* [2006] previously estimated that ~50% of the newly formed deep waters volume could be trapped into SCVs (anticyclonic or cyclonic).

Many parameters can influence the number and characteristics of the vortical structures formed during a deep convection event, such as the volume of newly formed deep waters, but also the timing and intensity of successive vertical mixing and restratification episodes. Deep convection is indeed a complex phenomenon controlled by both atmospheric forcing and oceanic preconditioning subjected to an important interannual variability [*Mertens and Schott*, 1998; *Somot et al*., 2016]. During this study period, in situ data describe four episodes of bottom-reaching mixing with approximately the same duration in the Gulf of Lions and intermediate mixing associated with WIW or WDW in the Ligurian Sea (see Figure 6). Moreover, the surface concerned by the deepest mixing is found to be roughly similar (~15–20 10^3 km^2), as shown by ocean color images [*Durrieu de Madron et al*., 2013] (Houpert et al., submitted manuscript) and in situ observations [*Bosse*, 2015]. The four consecutive winters could then be assumed to have generated a similar number of vortices with, however, some different vortices formed in the Ligurian Sea: WIW anticyclones in 2010 and 2011a and WDW anticyclones in 2012 and 2013.

The observational data coverage statistically leads to a total mean production of 90 eddies per year (see Appendix C and Figure 9). The 25th and 75th percentiles, respectively, corresponds to 80 and 120 eddies. Given the relative numbers of observed eddies of each class (18 anticyclones, 25 cyclones), one would thus expect the formation of about 35–55 cyclones and about the same number of anticyclones. Among the anticyclones about half of them would be anticyclonic SCVs of WMDW and the other half of WIW or WDW. Concerning cyclones, about half of them would similarly be surface-intensified, whereas the other half would be depth-intensified.

4.3. The Spreading of nWMDW: Anticyclones Versus Cyclones

With a typical vertical extension of 1000 m and a radius of 7 km, 60–90 eddies transporting newly formed deep waters (excluding here WIW and WDW anticyclonic SCVs) would trap a volume of 9.2–14 $\times$ 10^{12} m^3. The volume of deep waters formed during a convective winter is a key parameter, but difficult to estimate using in situ observations. However, the recent effort in the NW Mediterranean enables several estimates of the production rate using different methods: 1.0, 1.0, and 1.7–2.0 Sv for the winters 2011–2013 [*Bosse*, 2015], and 1.8 Sv for winter 2013 [*Waldman et al*., 2016]. Coherently using ocean color images, *Durrieu de Madron et al*. [2013] estimated a production rate of 1 Sv for winter 2012, and Houpert et al.(submitted manuscript), respectively, 0.8 and 1.3 Sv for winters 2010 and 2012. Considering a mean annual deep water production of 1.2 Sv for the study period, 24–37% of the total volume of newly formed deep waters would then be trapped in anticyclonic and cyclonic eddies. Despite the broad assumptions made to get this estimate, it agrees well with the 40–50% estimated by *Testor and Gascard* [2006], and the 30% by *Damien* [2015] from a high-resolution regional numerical simulation.

The relative importance of cyclones versus anticyclones is certainly dependent on the maximum depth reached by wintertime mixing. The formation of cyclonic structures is likely favored by bottom-reaching convection, while in case deep convection does not hit the bottom, it is much likely to observe anticyclonic SCVs. Bottom-reaching convection was a specificity of the Gulf of Lions region for the study period that could explain their relative abundance: 25 cyclones were observed, as compared to nine anticyclonic SCVs of deep waters. In other open-ocean deep convection sites such as the Labrador and Irminger Seas, cyclonic eddies have not yet been observed to be important in the spreading of the convected waters as have anticyclonic SCVs [*Gascard et al*., 2002; *Lilly and Rhines*, 2002; *Bower et al*., 2013]. This could be because deep convection apparently has not reached the bottom in those areas during the recent period [*De Jong et al*., 2012; *Piron et al*., 2015], or simply because high-latitude convection sites have been less intensively observed compared to the recent intense sampling of the Gulf of Lions. Numerical studies pointed out the role of hetons, dipoles consisting of a surface cyclone and a subsurface anticyclone, in the mixed waters

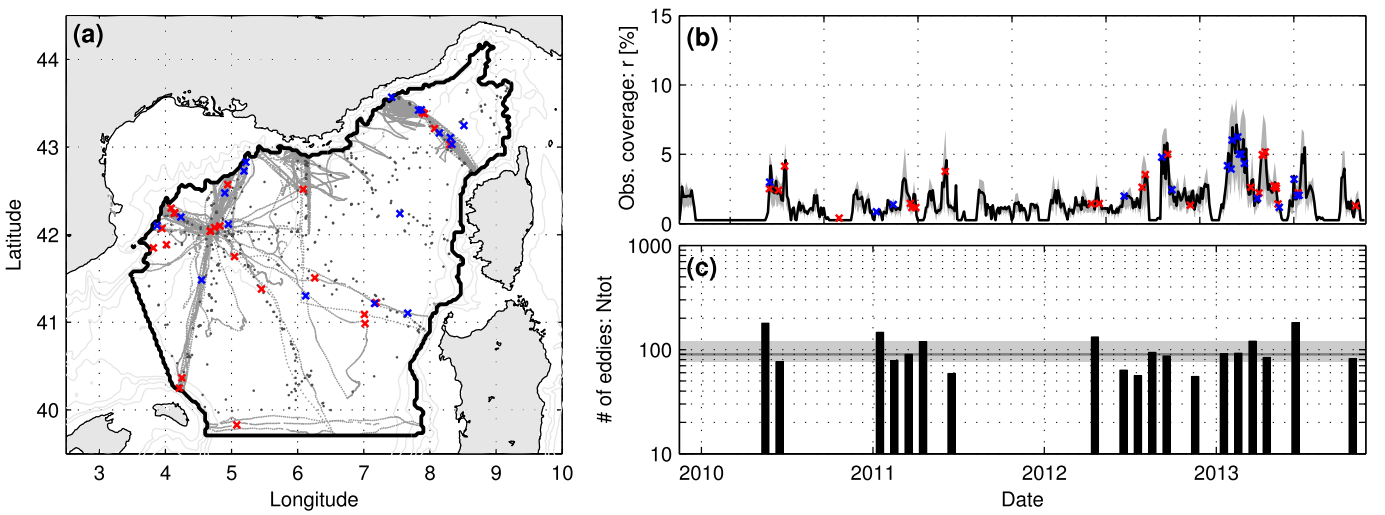

Figure 9. (a) Map of open-ocean observations in the north-western Mediterranean Sea from November 2009 to October 2013 by R/Vs (in gray) and gliders (in light gray). The location where vortices have been observed is colored in blue for anticyclones and in red for cyclones. The upper plot (b) shows the percentage of the basin surface covered by in situ observations for the study period with colored markers corresponding to vortices observations. The lower plot (c) represents an estimate of the number of eddies located within the basin (i.e., the number of observed eddies divided by the monthly in situ data coverage) whose median value is shown by the gray line and 25th–75th percentile interval by the gray shaded area.

spreading [*Hoog and Stommel*, 1985; *Legg and Marshall*, 1993]. They could act as effective spreading agents generated by baroclinic instability [*Legg et al*., 1996], before at last separating into surface cyclones and anticyclonic SCVs [*Oliver et al*., 2008]. Evidence of such dipolar structures remains, however, difficult to establish from in situ observations.

In the NW Mediterranean, numerical studies have pointed out the role of cyclonic eddies in the export of newly formed deep waters [*Herrmann et al*., 2008; *Beuvier et al*., 2012]. *Herrmann et al*. [2008] found that about one-third of the newly formed deep waters is exported southward by such cyclonic structures. In those simulations, the cyclones are large mesoscale surface-intensified cyclones lacking realistic characteristics, certainly because of a too coarse model resolution: 3 km in *Herrmann et al*. [2008] and 6–8 km in *Beuvier et al*. [2012]. To correctly resolve 5 km radius SCVs, a horizontal resolution of 1 km as in *Damien* [2015] seems to be needed.

4.4. Cascading Eddies

Dense waters overflow off continental shelves (cascading) is one of the important processes contributing to shelf-deep ocean exchanges (see *Ivanov et al*. [2004] and *Durrieu de Madron et al*. [2005] for a review of this phenomenon). Those dense waters are formed by cooling and evaporation (or by freezing and salinization) on a shallow shelf which then spill over the shelf edge as intense near-bottom gravity currents. Depending on their density anomaly, the cascading buoyant plume can either reach the abyssal plain or intermediate depths. In the Gulf of Lions, major cascading events occurred twice in the last decade and had great impacts on the bottom layers turbidity [*Puig et al*., 2013]. In 2012, moored current meters revealed intense currents within submarine canyons (up to 1 m s^{-1}) transporting relatively cold and fresh waters [*Durrieu de Madron et al*., 2013]. Two months after the cascading events, their signature appeared near the bottom at the LION mooring line (see location in Figure 1), indicating a swift spreading of cascading waters toward the basin interior. *Durrieu de Madron et al*. [2013] further used the basin-scale network of CTD casts collected during the MOOSE-GE cruise in July 2012 to map the thickness of this bottom layer (200 m on average) and revealed two peculiar stations associated with cascading waters extending to more than 1000 m above the seabed. In this study, the isopycnal deformation related to these bottom waters anomalies were identified as depth-intensified cyclones (C_5 and C_6 in Table 2, see also Figure 8c). In addition, a remarkable cold ($\theta \sim 12.82^{\circ}$C) and fresh ($S \sim 38.47$) signal at the bottom embedded within an intense cyclonic rotation (velocity max $>$15 cm s^{-1}) passed through the LION mooring in April 2012 (see Figure 5a). This is a striking evidence that cascading events can be trapped into intense coherent cyclonic eddies. Numerical studies recently illustrated the formation of cyclonic structures under similar conditions by shelf cascading East of Greenland [*Magaldi and Haine*, 2014] and off Cape Darnley, East Antarctica [*Nakayama et al*., 2014]. The

relation between cascading and its interaction with the mean circulation would need to be clarified in the context of eddy generation.

In 2012, three cyclones of cascading waters were observed among a total of six (see Table 2): C_6^* characterized by a very marked bottom core of SCDW, C_5 and C_6 having a less marked core that could result from the mixing with the surrounding WMDW. Assuming cyclones characterized by a ~500 m thick layer of cascading waters (see Figure 5a), and given the relatively small amount of dense waters produced on the shelf (0.1 Sv in 2012 estimated by *Durrieu de Madron et al*. [2013]), one single cyclone could transport 2.5% of the SCDW produced on the shelf.

5. Summary and Conclusion

This study examined the vertical structure and dynamical characteristics of vortices formed by deep convection in the northwestern Mediterranean based on in situ observations collected by R/Vs, a mooring line and autonomous gliders during the 2009–2013 period.

In total, 18 small (5–8 km) and intense (15–20 cm s^{-1}) subsurface anticyclonic eddies characterized by a homogeneous core associated with different water masses formed by deep vertical mixing were identified. In the Gulf of Lions, where the mixing is observed to reach the bottom each winter for this study period, the mixed patch had θ/S characteristics close to the Western Mediterranean Deep Waters (WMDW), whereas in the eastern part of the basin (the Ligurian Sea) intermediate mixing was observed. Winter Intermediate Waters (WIW) or Winter Deep Waters (WDW) was mainly formed there. This latter water mass observed between 500 and 1000 m depth with rather warm (>13.1°C) and salty (>38.5) characteristics due to the mixing of the Levantine Intermediate Waters has not been identified before. WDW is formed only when the vertical mixing reaches about 500–1000 m depths, which was the case in the Ligurian Sea during winters 2012 and 2013, but also in the Gulf of Lions recently in 2014 and 2015 [*Bosse*, 2015]. This study shows the importance to consider this distinct water masses apart from the lighter fresher WIW, and the denser colder WMDW in order to correctly characterize the deep mixing in the NW Mediterranean Sea.

Numerous cyclonic structures were also observed (25 in total), all characterized by a dense anomaly in the deep levels. Given their orbital velocity structure and associated isopycnal deformation, two categories were identified: (1) cyclones having peak velocities (15 cm s^{-1}) located near the surface with a radius of about 8 km; (2) smaller cyclones (6 km) with peak velocities slightly less intense (10 cm s^{-1}), but located well below the pycnocline. The first category corresponds to cones of convected waters extending to the surface described in previous numerical and laboratory studies [*Jones and Marshall*, 1993; *Maxworthy and Narimousa*, 1994]. Cyclones of the second category are characterized by an isopycnal pinching at the depth of their velocity maximum located between 500 m and sometimes more than 1000 m.

All these anticyclonic and cyclonic vortices have high Rossby numbers of $\pm$(0.3–0.6) that testify to a strong nonlinear dynamics. They were observed all year round and over the whole basin. These energetic circulation features generally prevail over the large-scale geostrophic circulation and remain coherent for long periods of time (typically 1 year). Anticyclonic eddies are formed by the dynamical adjustment of convected water parcels and belong to Submesoscale Coherent Vortices (SCVs) [*McWilliams*, 1985]. Also presented here are the first observations of long-lived deep cyclonic eddies that could be also considered as cyclonic SCVs considering their coherent nature, small radius and large aspect ratio with a Burger number close to one. Indeed, there is a duality between anticyclonic SCVs and depth-intensified cyclones having opposite effects on the potential vorticity (PV) field: anticyclones (resp., cyclones) are local PV minima (reps., maxima) due to their negative (resp., positive) relative vorticity and local stratification decrease (resp., increase) at the depth of their peak velocity.

From 2010 to 2013, every winter was characterized by strong bottom-reaching deep convection in the Gulf of Lions. Each winter, deep waters denser than the older ones were formed (Houpert et al., submitted manuscript). This specificity could have favored the generation of cyclonic eddies during the study period. The maximum depth reached by the deep convection (as well as the area over which deep convection reaches the bottom) certainly influences the predominance of cyclonic versus anticyclonic structures during the spreading phase of the newly formed deep waters. The spreading of 20–35% of the newly formed deep

waters was found to be driven by coherent vortical structures in accordance with previous rough estimates [*Testor and Gascard*, 2006].

Finally, coherent cyclones transporting cascading waters from the Gulf of Lions shelf have been identified a few months after the cascading event of winter 2012. As a relative small volume of dense waters is thought to be formed on the shelf (0.1 Sv in 2012 according to *Durrieu de Madron et al*. [2013]), those vortical structures could thus easily transport a significant fraction of it and have further implications like the transport of sediments over long distances.

The scales and dynamics of vortical structures generated by deep convection in the NW Mediterranean Sea were here thoroughly analyzed, complementing previous studies by *Testor and Gascard* [2003, 2006] using Lagrangian RAFOS floats that were not able to document their vertical structure. The present study was made possible through the regular and intense use of autonomous gliders along specified endurance lines mainly realized in the framework of the MOOSE project, an ocean observing system dedicated to the monitoring of the NW Mediterranean Sea. This long-term strategy also enabled to identify SCVs of warm and salty LIW [*Bosse et al*., 2015], thus demonstrating its additional relevance to conduct process studies with gliders.

The numerous observations and variety of Submesoscale Coherent Vortices confirm their prominent role for the deep and intermediate waters dynamics. The quantification of their role in the deep convection preconditioning and the basin-scale spreading of tracers (both physical and biogeochemical) are important issues that need to be assessed in the future. To this end, high-resolution numerical models could be used. The impacts of SCVs could eventually be parameterized in coarse resolution climate models that are still far from being able to resolve them. Biogeochemical observations at the small scale associated with SCVs are also a real challenge, but needed to improve our comprehension of the rapidly changing Mediterranean Sea in the context of climate change.

Appendix A: Solving the Gradient Wind Balance With Gliders

For small-scale vortices characterized by relatively strong horizontal shear ($>0.1f$), the force balance becomes ageostrophic because of nonlinear effects (i.e., the centrifugal force). This latter force needs to be taken into account, otherwise, the velocity is underestimated for anticyclones and overestimated for cyclones [*Elliott and Sanford*, 1986; *Penven et al*., 2014]. The cyclostrophic velocities v_c can be retrieved by solving the quadratic equation expressing the gradient wind balance in a cylindrical coordinate system:

$$\frac{v_c^2(r,z)}{r}+fv_c(r,z)=fv_g(r,z) \tag{A1}$$

with r the distance to the eddy center, z the depth, f the Coriolis parameter, and v_g the geostrophic velocity field. Keeping the relevant solution from equation (A1) then yields:

$$v_c(r,z)=\frac{rf}{2}\times\left(-1+\sqrt{1+4\frac{v_g(r,z)}{rf}}\right) \tag{A2}$$

To infer cyclostrophic velocities, (1) the eddy center position and (2) absolute geostrophic velocities have to be determined.

(1) Vortex Center Detection

As in *Bosse et al*. [2015], glider depth-average currents (minus a mean advection) are used as an indicator of the eddy velocity field in the horizontal plane. A mean advection is defined by averaging the DAC within a running window of ±1 day and ±25 km which accounts for the large-scale circulation features. In order to position the eddy center, the following cost function is minimized: $g(x,y)=1/n\sum_{i=1}^{n}[\mathbf{v_i}\cdot\mathbf{r_i}(x,y)/||\mathbf{r_i}(x,y)||]^2$ with (x, y) a given position in the horizontal plane, $\mathbf{r_i}(x,y)/||\mathbf{r_i}(x,y)||$ the normalized vector linking (x, y) to the location where the depth-average velocities $\mathbf{v_i}$ are estimated. We choose $n = 4$ centered around each vortex center to preserve the synoptic character of the sampling (see Figure 7 in *Bosse et al*. [2015] for an illustration of this cost function method).

(2) Geostrophic Velocities

The cross-track geostrophic vertical shear is computed by integrating the thermal wind balance from a smoothed density section. A low-pass filter is first applied to filter out small-scale isopycnals oscillations mostly due to the aliased sampling of internal waves without fading the signature of the eddies. The cutoff length scale is set by the internal deformation radius, the scale at which geostrophy can be considered as valid. A modal decomposition on typical density profiles yields a first baroclinic deformation radius of about 6 km. This is relatively small compared to other oceans owing to the low stratification of the northwestern Mediterranean Sea. As in *Bosse et al*. [2015], the cross-track potential density is filtered using a Gaussian moving average of 2 km variance (significant width of about 6 km).

In this study, a novel method is used to compute the geostrophic component from the measured DAC and the geostrophic shear. Geostrophic and cyclostrophic velocities can be decomposed into a depth-average and a depth-varying (baroclinic) component: $v(r,z)=\bar{v}(r)+v\prime(r,z)$ with $\bar{v}(r)=\frac{1}{H}\int_{-H}^{0}v(r,z)\mathrm{d}z$ and $\frac{1}{H}\int_{-H}^{0}v\prime(r,z)\mathrm{d}z=0$ (H being the maximum depth reached by a glider, usually 1000 m). Averaging equation (A2) over z then yields:

$$\frac{2\overline{v_c}(r)}{rf}=-1+\frac{1}{H}\int_0^H\sqrt{1+\frac{4\overline{v_g}(r)}{rf}+\frac{4v\prime_g(r,z)}{rf}}\mathrm{d}z \tag{A3}$$

In this equation, $\overline{v_c}(r)$ corresponds to the total depth-average velocity estimated by the glider, $\overline{v_g}(r)$ to the unknown geostrophic depth-average velocity and $v\prime_g(r,z)$ to the geostrophic shear that can be computed from the thermal wind balance, as previously described.

The equation (A3) is solved for each eddy to retrieve $\overline{v_g}(r)$, which is then used to properly reference the absolute geostrophic orbital velocities. Note that ageostrophy is assumed to be mostly due to the centrifugal force and eddies are circular. As expected, the geostrophic depth-average orbital velocities are smaller (resp., larger) in magnitude for anticyclones (resp., cyclones) than the total ones. The correction corresponds to about 10–20% of the total velocity magnitude, and therefore must be taken into account.

Finally, cyclostrophic velocities can simply be computed using equation (A2).

As gliders did not cross each eddy right through its center, the following equations are solved in the glider coordinate system. The apparent eddy radius and orbital peak velocities are then geometrically corrected by a factor $\epsilon=\sqrt{1+d^2/R^2}$ with d the distance between the glider track and the estimated eddy center, as done in *Bosse et al*. [2015].

Appendix B: Considerations About the Columnar Buoyancy

Let us consider a water column whose stratification is given by $N^2(z)$ at a given time t_0 with $N^2(z)=0$ for $0<z<z_0$, z_0 being the initial mixed layer depth. For simplicity, we neglect the horizontal advection and assume that nonpenetrative vertical mixing caused by a surface buoyancy flux B_s between t_0 and t deepens the mixed layer from z_0 to $z(t)$. In this situation, after an integration by parts of equation (9.2.5) in *Turner* [1973] (see also *Lascaratos and Nittis* [1998]), one has:

$$IS(z(t))=\int_{z_0}^{z(t)}N^2(z\prime)z\prime\mathrm{d}z\prime=\int_{t_0}^{t}B_s(t\prime)\mathrm{d}t\prime \tag{B1}$$

where $IS(z(t))$ represents the stratification index introduced by *Herrmann et al*. [2008]. The mixed layer deepening through time is then given by

$$\frac{\mathrm{d}z}{\mathrm{d}t}=B_s(t)\times\left[\frac{\mathrm{d}IS}{\mathrm{d}z}\right]^{-1}=\frac{B_s(t)}{N^2(z)z} \tag{B2}$$

The spatial scale associated with oceanic submesoscale eddies (~10 km) being much smaller than that of the atmospheric forcing (~100–1000 km), it is thus reasonable to assume the buoyancy loss $B_s(t)$ to be spatially homogeneous over the eddies and their surrounding waters. In order to discuss the eddy effect on the mixed layer deepening, we define Γ the mixed layer deepening ratio, as

$$\Gamma(z)=\frac{\mathrm{d}z}{\mathrm{d}t}\Big|_{scv}\Big/\frac{\mathrm{d}z}{\mathrm{d}t}\Big|_{out}=\frac{\mathrm{d}IS}{\mathrm{d}z}\Big|_{out}\Big/\frac{\mathrm{d}IS}{\mathrm{d}z}\Big|_{scv}=\frac{N^2_{out}(z)}{N^2_{scv}(z)} \tag{B3}$$

Appendix C: Statistical Eddy Census

Let us assume N_{tot} eddies of radius R_m to randomly move at a speed v_a in an oceanic basin. On a time scale of $\delta t=2R_m/v_a$, the eddies will have moved to new random positions. In the mean time, the number of observed eddies n_{obs} is proportional to the surface covered by in situ observations: $N_{tot}=n_{obs}/r$ with r being the ratio of the data coverage to the basin surface.

During the study period, the in situ data coverage can be estimated for each time interval of δt by considering the sampling area of individual profiles. The eddies radius R_m is defined here as the distance between the center and the velocity maximum, but orbital velocities generally decrease to zero within a larger distance and the hydrographical signature generally extends a bit further one radius (about to $1.5R_m$). A numerical study by *Ciani et al.* [2016] recently estimated the critical merger distance for subsurface anticyclone. Accordingly, the minimum distance separating two eddies before they merge or collapse will be assumed to be $2.5\times\sqrt{2}R_m$. For profiles taken inside an eddy core, the sampling area will be a disk of about $2R_m$ radius. For any ordinary profile (with no hydrographical eddy signature), the closest eddy center could be possibly at a distance of $1.5R_m$. The sampling area will thus be a disk of $1.5R_m$ radius. Following these assumptions, the in situ data coverage can be estimated and divided by the basin surface to compute the parameter r. The total number of eddies ($N_{tot}=n_{obs}/r$) is eventually estimated by averaging r over a month (the typical duration of a research cruise or a glider mission) and by counting the number of observed eddies.

This statistical method is here applied with the following parameters: $R_m=7.0\pm1.3$ km and $v_a=5.5\pm2.5$ cm s^{-1} (leading to $\delta t=2.9\pm1.9$ days). The result can be seen in Figure 9 and are discussed in section 4.2.

Two main limitations of our statistical considerations are the fact that: (1) the number of eddies within a large oceanic basin may vary with time, as eddies are dissipated, formed or exit the delimited domain; (2) the observational data coverage is very sensitive to effective hydrographical eddy radius (chose here as $1.5R_m$). However, the result should not be affected by the fact that a single eddy could have been sampled twice (as it is the case for eddies A_4^{wdw} and A_5^{wdw}).

Acknowledgments

The hydrographical data were collected and made freely available by the Coriolis project and programmes that contribute to it (http://www.coriolis.eu.org). We would like to acknowledge the staff of the National Pool of Gliders of DT-INSU for the sustained gliders deployments. Captains, crew members of *R/V Le Tethys II* (INSU), *R/V L'Atalante* (Ifremer) and *R/V Le Suroit* (Ifremer), as well as scientists who participated to the MOOSE-GE, CASCADE, DEWEX, and DOWEX different cruises are also warmly thanked. Support was provided by the French MISTRALS program (HyMeX and MERMeX components), the MOOSE project (AllEnvi-INSU long-term observatory, http://www.moose-network.fr), the French Bio-Argo project (CNES-TOSCA) and the French NAOS project (ANR J11R107-F), as well as by the FP7 EU projects GROOM (Grant agreement 284321), PERSEUS (Grant agreement 287600), and JERICO (Grant agreement 262584), and the EGO-COST Action ES0904. A. Bosse was funded by a French government scholarship.

References

Andres, M., J. M. Toole, D. J. Torres, W. M. Smethie, T. M. Joyce, and R. G. Curry (2015), Stirring by deep cyclones and the evolution of Denmark strait overflow water observed at line W, *Deep Sea Res., Part I*, *109*, 10–26, doi:10.1016/j.dsr.2015.12.011.

Armi, L., D. Hebert, N. Oakey, J. F. Price, P. L. Richardson, T. Rossby, and B. Ruddick (1988), The history and decay of a Mediterranean salt lens, *Nature*, *333*, 649–651, doi:10.1038/333649a0.

Béthoux, J.-P., X. Durieu de Madron, F. Nyffeler, and D. Tailliez (2002), Deep water in the western Mediterranean: Peculiar 1999 and 2000 characteristics, shelf formation hypothesis, variability since 1970 and geochemical inferences, *J. Mar. Syst.*, *33–34*, 117–131, doi:10.1016/S0924-7963(02)00055-6.

Beuvier, J., K. Béranger, C. Lebeaupin Brossier, S. Somot, F. Sevault, Y. Drillet, R. Bourdallé-Badie, N. Ferry, and F. Lyard (2012), Spreading of the Western Mediterranean Deep Water after winter 2005: Time scales and deep cyclone transport, *J. Geophys. Res.*, *117*, C07022, doi:10.1029/2011JC007679.

Bosse, A. (2015), Circulation générale et couplage physique-biogéochimie à (sous-)mésoéchelle en Méditerranée Nord-occidentale à partir de données in situ, PhD thesis, Univ. Pierre et Marie Curie, Paris.

Bosse, A., P. Testor, L. Mortier, L. Prieur, V. Taillandier, F. D'Ortenzio, and L. Coppola (2015), Spreading of Levantine Intermediate Waters by submesoscale coherent vortices in the northwestern Mediterranean Sea as observed with gliders, *J. Geophys. Res. Oceans*, *120*, 1599–1622, doi:10.1002/2014JC010263.

Bouffard, J., A. Pascual, S. Ruiz, Y. Faugère, and J. Tintoré (2010), Coastal and mesoscale dynamics characterization using altimetry and gliders: A case study in the Balearic Sea, *J. Geophys. Res.*, *115*, C10029, doi:10.1029/2009JC006087.

Bouffard, J., L. Renault, S. Ruiz, A. Pascual, C. Dufau, and J. Tintoré (2012), Sub-surface small-scale eddy dynamics from multi-sensor observations and modeling, *Prog. Oceanogr.*, *106*, 62–79, doi:10.1016/j.pocean.2012.06.007.

Bower, A. S., R. M. Hendry, D. E. Amrhein, and J. M. Lilly (2013), Direct observations of formation and propagation of subpolar eddies into the subtropical North Atlantic, *Deep Sea Res., Part II*, *85*(July), 15–41.

Bubnov, B. M., and G. S. Golitsyn (1985), Convection modes in a rotating fluid, *Dokl. Akad. Nauk SSSR*, *281*, 552–555.

Carpenter, J. R., and M.-L. Timmermans (2012), Deep mesoscale eddies in the Canada Basin, Arctic Ocean, *Geophys. Res. Lett.*, *39*, L20602, doi:10.1029/2012GL053025.

Carton, X., L. Chérubin, J. Paillet, Y. Morel, A. Serpette, and B. Le Cann (2002), Meddy coupling with a deep cyclone in the Gulf of Cadiz, *J. Mar. Syst.*, *32*(1–3), 13–42, doi:10.1016/S0924-7963(02)00028-3.

Ciani, D., X. Carton, and J. Verron (2016), On the merger of subsurface isolated vortices, *Geophys. Astrophys. Fluid Dyn.*, *110*(1), 23–49, doi:10.1080/03091929.2015.1135430.

Conan, P. (2013), DEWEX-MERMEX 2013 LEG2 cruise, RV Le Suroît, *Tech. Rep.*, doi:10.17600/13020030.

Crépon, M., L. Wald, and J. M. Monget (1982), Low-frequency waves in the Ligurian Sea during December 1977, *J. Geophys. Res.*, *87*(Ci), 595–600.
Damien, P. (2015), Étude de la circulation océanique en Méditerranée Occidentale à l'aide d'un modèle numérique à haute résolution: Influence de la submésoéchelle, PhD thesis, Univ. Toulouse 3 Paul Sabatier, Toulouse, France.
D'Asaro, E. (1988a), Observations of small eddies in the Beaufort Sea, *J. Geophys. Res.*, *93*(C6), 6669–6684.
D'Asaro, E. (1988b), Generation of submesoscale vortices: A new mechanism, *J. Geophys. Res.*, *93*(C6), 6685.
Davis, R. E., M. D. Ohman, D. L. Rudnick, J. T. Sherman, and B. A. Hodges (2008), Glider surveillance of physics and biology in the southern California Current System, *Limnol. Oceanogr.*, *53*(5, Part 2), 2151–2168, doi:10.4319/lo.2008.53.5_part_2.2151.
De Jong, M. F., H. M. Van Aken, K. Våge, and R. S. Pickart (2012), Convective mixing in the central Irminger Sea: 2002–2010, *Deep Sea Res, Part I*, *63*, 36–51, doi:10.1016/j.dsr.2012.01.003.
Drobinski, P., et al. (2014), HYMEX: A 10-year multidisciplinary program on the Mediterranean water cycle, *Bull. Am. Meteorol. Soc.*, *95*(7), 1063–1082, doi:10.1175/BAMS-D-12-00242.1.
Durrieu de Madron, X. (2011), CASCADE cruise, RV L'Atalante, *Tech. Rep.*, doi:10.17600/11010020.
Durrieu de Madron, X., V. Zervakis, A. Theocharis, and D. Georgopoulos (2005), Comments on Cascades of dense water around the world ocean, *Prog. Oceanogr.*, *64*(1), 83–90, doi:10.1016/j.pocean.2004.08.004.
Durrieu de Madron, X., et al. (2011), Marine ecosystems' responses to climatic and anthropogenic forcings in the Mediterranean, *Prog. Oceanogr.*, *91*(2), 97–166, doi:10.1016/j.pocean.2011.02.003.
Durrieu de Madron, X., et al. (2013), Interaction of dense shelf water cascading and open-sea convection in the northwestern Mediterranean during winter 2012, *Geophys. Res. Lett.*, *40*, 1379–1385, doi:10.1002/grl.50331.
Elliott, B. A., and T. B. Sanford (1986), The subthermocline lens D1. Part II: Kinematics and dynamics, *J. Phys. Oceanogr.*, *16*(3), 549–561, doi: 10.1175/1520-0485(1986)016 < 0549:TSLDPI>2.0.CO;2.
Ertel, H. (1942), Ein neuer hydrodynamischer wirbelsatz, *Meteorol. Z.*, *59*, 277–281.
Fan, X., U. Send, P. Testor, J. Karstensen, P. Lherminier, and G. Drive (2013), Observations of Irminger Sea anticyclonic eddies, *J. Phys. Oceanogr.*, *43*, 805–823, doi:10.1175/JPO-D-11-0155.1.
Garau, B., S. Ruiz, W. G. Zhang, A. Pascual, E. E. Heslop, J. Kerfoot, and J. Tintoré (2011), Thermal lag correction on Slocum CTD glider data, *J. Atmos. Oceanic Technol.*, *28*(9), 1065–1071, doi:10.1175/JTECH-D-10-05030.1.
Gascard, J.-C. (1978), Mediterranean deep water formation baroclinic instability and oceanic eddies, *Oceanol. Acta*, *1*(3), 315–330.
Gascard, J.-C., and R. A. Clarke (1983), The formation of Labrador Sea Water. Part II. Mesoscale and smaller-scale processes, *J. Phys. Oceanogr.*, *13*, 1779–1797, doi:10.1175/1520-0485(1983)013 < 1779:TFOLSW>2.0.CO;2.
Gascard, J.-C., A. J. Watson, M.-J. Messias, K. A. Olsson, T. Johannessen, and K. Simonsen (2002), Long-lived vortices as a mode of deep ventilation in the Greenland Sea, *Nature*, *416*, 525–527.
Gasparini, G., G. Zodiatis, M. Astraldi, C. Galli, and S. Sparnocchia (1999), Winter intermediate water lenses in the Ligurian Sea, *J. Mar. Syst.*, *20*(1–4), 319–332, doi:10.1016/S0924-7963(98)00089-X.
Gourdeau, L., W. S. Kessler, R. E. Davis, J. T. Sherman, C. Maes, and E. Kestenare (2008), Zonal jets entering the Coral Sea, *J. Phys. Oceanogr.*, *38*, 715–725, doi:10.1175/2007JPO3780.1.
Griffiths, R. W., and P. F. Linden (1981), The stability of vortices in a rotating, stratified fluid, *J. Fluid Mech.*, *105*, 283–316.
Herrmann, M. J., S. Somot, F. Sevault, C. Estournel, and M. Déqué (2008), Modeling the deep convection in the northwestern Mediterranean sea using an eddy-permitting and an eddy-resolving model: Case study of winter 1986–1987, *J. Geophys. Res.*, *113*, C04011, doi:10.1029/2006JC003991.
Hoog, N. G., and H. M. Stommel (1985), Hetonic explosions: The breakup and spread of warm pools as explained by baroclinic point vortices, *J. Atmos. Sci.*, *42*(14), 1465–1476, doi:10.1175/1520-0469(1985)042 < 1465:HETBAS>2.0.CO;2.
Houpert, L. (2013), Contribution to the study of transfer processes from the surface to the deep ocean in the Mediterranean Sea using in situ Measurements, PhD thesis, Univ. de Perpignan.
Høydalsvik, F., C. Mauritzen, K. A. Orvik, J. H. LaCasce, C. M. Lee, and J. Gobat (2013), Transport estimates of the Western Branch of the Norwegian Atlantic Current from glider surveys, *Deep Sea Res., Part I*, *79*(0), 86–95, doi:10.1016/j.dsr.2013.05.005.
Ivanov, V. V., G. I. Shapiro, J. M. Huthnance, D. L. Aleynik, and P. N. Golovin (2004), Cascades of dense water around the world ocean, *Prog. Oceanogr.*, *60*(1), 47–98, doi:10.1016/j.pocean.2003.12.002.
Jones, H., and J. Marshall (1993), Convection with rotation in a neutral ocean: A study of open-ocean deep convection, *J. Phys. Oceanogr.*, *23*, 1009–1039, doi:10.1175/1520-0485(1993) 023 < 1009:CWRIAN>2.0.CO;2.
Jones, H., and J. Marshall (1997), Restratification after deep convection, *J. Phys. Oceanogr.*, *27*, 2276–2287, doi:10.1175/1520-0485(1997)027 < 2276:RADC>2.0.CO;2.
Julien, K., S. Legg, J. McWilliams, and J. Werne (1996), Rapidly rotating turbulent Rayleigh-Bknard convection, *J. Fluid Mech.*, *322*, 243–273, doi:10.1017/S0022112096002789.
Juza, M., L. Renault, S. Ruiz, and J. Tintoré (2013), Origin and pathways of Winter Intermediate Water in the Northwestern Mediterranean Sea using observations and numerical simulation, *J. Geophys. Res. Oceans*, *118*, 6621–6633, doi:10.1002/2013JC009231.
Killworth, P. D. (1983), Deep convection in the world ocean, *Rev. Geophys. Space Phys.*, *21*(1), 1–26.
Kloosterziel, R. C., G. F. Carnevale, and P. Orlandi (2007), Inertial instability in rotating and stratified fluids: Barotropic vortices, *J. Fluid Mech.*, *583*, 379–412, doi:10.1017/S0022112007006325.
Lascaratos, A., and K. Nittis (1998), A high-resolution three-dimensional numerical study of intermediate water formation in the Levantine Sea, *J. Geophys. Res.*, *103*(C9), 18,497–18,511.
Lazar, A., A. Stegner, and E. Heifetz (2013), Inertial instability of intense stratified anticyclones. Part 1. Generalized stability criterion, *J. Fluid Mech.*, *732*, 457–484, doi:10.1017/jfm.2013.412.
Leaman, K. D., and F. A. Schott (1991), Hydrographic structure of the convection regime in the Gulf of Lions: Winter 1987, *J. Phys. Oceanogr.*, *21*(4), pp. 575–598, doi:10.1175/1520-0485(1991)021 < 0575:HSOTCR>2.0.CO;2.
Legg, S., and J. C. Marshall (1993), A heton model of the spreading phase of open-ocean deep convection, *J. Phys. Oceanogr.*, *23*, pp. 1040–1056, doi:10.1175/1520-0485(1993)023 < 1040:AHMOTS>2.0.CO;2.
Legg, S., H. Jones, and M. Visbeck (1996), A heton perspective of baroclinic eddy transfer in localized open ocean convection, *J. Phys. Oceanogr.*, *26*, 2251–2266.
Legg, S., J. McWilliams, and J. Gao (1998), Localization of deep ocean convection by a mesoscale eddy, *J. Phys. Oceanogr.*, *28*, 944–970, doi: 10.1175/1520-0485(1998)028 < 0944:LODOCB>2.0.CO;2.
L'Hégaret, P., X. Carton, S. Louazel, and G. Boutin (2016), Mesoscale eddies and submesoscale structures of Persian Gulf Water off the Omani coast in spring 2011, *Ocean Sci.*, *12*(3), 687–701, doi:10.5194/os-12-687-2016.

Lherminier, P., J.-C. Gascard, and D. Quadfasel (1999), The Greenland Sea in water 1993 and 1994: Preconditioning for deep convection, *Deep Sea Res., Part II*, *46*(67), 1199–1235, doi:10.1016/S0967-0645(99)00020-X.
Lilly, J. M., and P. B. Rhines (2002), Coherent eddies in the Labrador Sea observed from a mooring, *J. Phys. Oceanogr.*, *32*(2), 585–598, doi:10.1175/1520-0485(2002)032 < 0585:CEITLS>2.0.CO;2.
Magaldi, M. G., and T. W. N. Haine (2014), Hydrostatic and non-hydrostatic simulations of the East Greenland Spill Jet, *Deep Sea Res., Part I*, *14*, 13,372, doi:10.1016/j.dsr.2014.10.008.
Marshall, J., and F. Schott (1999), Open-ocean convection: Observations, theory, and models, *Rev. Geophys.*, *37*(1), 1–64, doi:10.1029/98RG02739.
Martin, J. P., C. M. Lee, C. C. Eriksen, C. Ladd, and N. B. Kachel (2009), Glider observations of kinematics in a Gulf of Alaska eddy, *J. Geophys. Res.*, *114*, C12021, doi:10.1029/2008JC005231.
Marty, J.-C., and J. Chiavérini (2010), Hydrological changes in the Ligurian Sea (NW Mediterranean, DYFAMED site) during 19952007 and biogeochemical consequences, *Biogeosciences*, *7*(7), 2117–2128, doi:10.5194/bg-7-2117-2010.
Maxworthy, T., and S. Narimousa (1994), Unsteady, turbulent convection into a homogeneous, rotating fluid, with oceanographic applications, *J. Phys. Oceanogr.*, *24*(5), 865–887, doi:10.1175/1520-0485(1994)024 < 0865:UTCIAH>2.0.CO;2.
McWilliams, J. C. (1985), Submesoscale, coherent vortices in the ocean, *Rev. Geophys.*, *23*(2), 165, doi:10.1029/RG023i002p00165.
McWilliams, J. C. (1988), Vortex generation through balanced adjustment, *J. Phys. Oceanogr.*, *18*, 1178–1192, doi:10.1175/1520-0485(1988)018 < 1178:VGTBA>2.0.CO;2.
McWilliams, J. C. (2016), Submesoscale currents in the ocean, *Proc. R. Soc. London A*, *472*(2189), doi:10.1098/rspa.2016.0117.
MEDOC-Group, T. (1970), Observation of formation of deep water in the Mediterranean Sea, 1969, *Nature*, *225*, 1037–1040, doi:10.1038/2271037a0.
Merckelbach, L. M., R. D. Briggs, D. A. Smeed, and G. Griffiths (2008), Current measurements from autonomous underwater gliders, in *Proceedings of the Ninth IEEE Working Conference on Current Measurement Technology*, pp. 61–67, doi:10.1109/CCM.2008.4480845.
Mertens, C., and F. Schott (1998), Interannual variability of deep-water formation in the Northwestern Mediterranean, *J. Phys. Oceanogr.*, *28*(7), 1410–1424, doi:10.1175/1520-0485(1998)028 < 1410:IVODWF>2.0.CO;2.
Millot, C. (1999), Circulation in the Western Mediterranean Sea, *J. Mar. Syst.*, *20*(1–4), 423–442, doi:10.1016/S0924-7963(98)00078-5.
Molemaker, M. J., J. C. McWilliams, and W. K. Dewar (2015), Submesoscale instability and generation of mesoscale anticyclones near a separation of the California undercurrent, *J. Phys. Oceanogr.*, *45*(3), 613–629, doi:10.1175/JPO-D-13-0225.1.
Mortier, L. (2012), DOWEX2012 cruise, RV Téthys II, *Tech. Rep.*, doi:10.17600/12450170.
Mortier, L., and V. Taillandier (2013), DOWEX2013 cruise, RV Téthys II, *Tech. Rep.*, doi:10.17600/13450150.
Nakayama, Y., K. I. Ohshima, Y. Matsumura, Y. Fukamachi, and H. Hasumi (2014), A numerical investigation of formation and variability of Antarctic bottom water off Cape Darnley, East Antarctica, *J. Phys. Oceanogr.*, *44*(11), 2921–2937, doi:10.1175/JPO-D-14-0069.1.
Oliver, K. I. C., T. Eldevik, D. P. Stevens, and A. J. Watson (2008), A Greenland Sea perspective on the dynamics of postconvective eddies, *J. Phys. Oceanogr.*, *38*, 2755–2771, doi:10.1175/2008JPO3844.1.
Pelland, N. A., C. C. Eriksen, and C. M. Lee (2013), Subthermocline eddies over the Washington continental slope as observed by Seagliders, 2003–09, *J. Phys. Oceanogr.*, *43*(10), 2025–2053, doi:10.1175/jpo-d-12-086.1.
Penven, P., I. Halo, S. Pous, and L. Marie (2014), Cyclogeostrophic balance in the Mozambique Channel, *J. Geophys. Res. Oceans*, *119*, 1054–1067, doi:10.1002/2013JC009528.
Pietri, A., P. Testor, V. Echevin, A. Chaigneau, L. Mortier, G. Eldin, and C. Grados (2013), Finescale vertical structure of the upwelling system off Southern Peru as observed from glider data, *J. Phys. Oceanogr.*, *43*(3), 631–646, doi:10.1175/JPO-D-12-035.1.
Pietri, A., V. Echevin, P. Testor, A. Chaigneau, L. Mortier, C. Grados, and A. Albert (2014), Impact of a coastal-trapped wave on the near-coastal circulation of the Peru upwelling system from glider data, *J. Geophys. Res. Oceans*, *119*, 2109–2120, doi:10.1002/2013JC009270.
Piron, A., V. Thierry, H. Mercier, and G. Caniaux (2015), Argo float observations of basin-scale deep convection in the Irminger Sea during winter 2011–2012, *Deep Sea Res., Part I*, *109*, 76–90, doi:10.1016/j.dsr.2015.12.012.
Poulain, P.-M., et al. (2007), MedArgo: A drifting profiler program in the Mediterranean Sea, *Ocean Sci.*, *3*(3), 379–395, doi:10.5194/os-3-379-2007.
Provenzale, A. (1999), Transport by coherent barotropic vortices, *Annu. Rev. Fluid Mech.*, *31*(1), 55–93, doi:10.1146/annurev.fluid.31.1.55.
Puig, P., et al. (2013), Thick bottom nepheloid layers in the western Mediterranean generated by deep dense shelf water cascading, *Prog. Oceanogr.*, *111*, 1–23, doi:10.1016/j.pocean.2012.10.003.
Rhines, P. B., and W. R. Young (1983), How rapidly is a passive scalar mixed within closed streamlines?, *J. Fluid Mech.*, *133*, 133–145, doi:10.1017/S0022112083001822.
Ronski, S., and G. Budéus (2006), Vertical structure reveals eddy lifetime in the Greenland Sea, *Geophys. Res. Lett.*, *33*, L11602, doi:10.1029/2006GL026045.
Savidge, D. K., and J. M. Bane (1999), Cyclogenesis in the deep ocean beneath the Gulf Stream: 1. Description, *J. Geophys. Res.*, *104*(C8), 18,111–18,126.
Schroeder, K., J. Chiggiato, H. L. Bryden, M. Borghini, and S. Ben Ismail (2016), Abrupt climate shift in the Western Mediterranean Sea, *Sci. Rep.*, *6*, 23,009, doi:10.1038/srep23009.
Send, U., and J. Marshall (1995), Integral effects of deep convection, *J. Phys. Oceanogr.*, *25*(5), 855–872, doi:10.1175/1520-0485(1995)025 < 0855:IEODC>2.0.CO;2.
Send, U., J. Font, and C. Mertens (1996), Recent observation indicates convection's role in deep water circulation, *Eos Trans. AGU*, *77*(7), 61–65.
Søiland, H., and T. Rossby (2013), On the structure of the Lofoten Basin eddy, *J. Geophys. Res. Oceans*, *118*, 4201–4212, doi:10.1002/jgrc.20301.
Somot, S., et al. (2016), Characterizing, modelling and understanding the climate variability of the deep water formation in the north-western Mediterranean sea, *Clim. Dyn.*, doi:10.1007/s00382-016-3295-0.
Spall, M. A., and J. F. Price (1998), Mesoscale variability in Denmark strait: The PV outflow hypothesis*, *J. Phys. Oceanogr.*, *28*(1969), 1598–1623, doi:10.1175/1520-0485(1998)028 < 1598:MVIDST>2.0.CO;2.
Testor, P. (2013), DEWEX-MERMEX 2013 LEG1 cruise, RV Le Suroît, *Tech. Rep.*, doi:10.17600/13020010.
Testor, P., and J.-C. Gascard (2003), Large-scale spreading of deep waters in the Western Mediterranean Sea by submesoscale coherent eddies, *J. Phys. Oceanogr.*, *33*, 75–87, doi:10.1175/1520-0485(2003)033 < 0075:LSSODW>2.0.CO;2.
Testor, P., and J.-C. C. Gascard (2006), Post-convection spreading phase in the Northwestern Mediterranean Sea, *Deep Sea Res., Part I*, *53*(5), 869–893, doi:10.1016/j.dsr.2006.02.004.
Testor, P., and L. Mortier (2010), MOOSE-GE 2010 cruise, RV Téthys II, *Tech. Rep.*, doi:10.17600/10450080.

Testor, P., et al. (2010), Gliders as a component of future observing systems, in *Proceedings of OceanObs'09: Sustained Ocean Observations and Information for Society (Vol. 2)*, edited by J. Hall, D. E. Harrison, and D. Stammer, *21–25 September 2009*, Venice, Italy, doi:10.5270/OceanObs09.cwp.89.

Testor, P., L. Coppola, and L. Mortier (2011), MOOSE-GE 2011 cruise, RV Téthys II, *Tech. Rep*., doi:10.17600/11450160.

Testor, P., L. Coppola, and L. Mortier (2012), MOOSE-GE 2012 cruise, RV Le Suroît, *Tech. Rep*., doi:10.17600/12020030.

Testor, P., L. Coppola, and L. Mortier (2013), MOOSE-GE 2013 cruise, RV Téthys II, *Tech. Rep*., doi:10.17600/13450110.

Thomsen, S., T. Kanzow, G. Krahmann, R. J. Greatbatch, M. Dengler, and G. Lavik (2016), The formation of a subsurface anticyclonic eddy in the peru-chile undercurrent and its impact on the near-coastal salinity, oxygen, and nutrient distributions, *J. Geophys. Res. Oceans*, *121*, 476–501, doi:10.1002/2015JC010878.

Timmermans, M.-L., J. Toole, R. Krishfield, and P. Winsor (2008), Ice-Tethered Profiler observations of the double-diffusive staircase in the Canada Basin thermocline, *J. Geophys. Res.*, *113*, C00A02, doi:10.1029/2008JC004829.

Turner, J. S. (1973), *Buoyancy Effects in Fluids*, Cambridge Univ. Press, Cambridge.

Vargas-Yáñez, M., et al. (2012), Extreme Western Intermediate Water formation in winter 2010, *J. Mar. Syst.*, *105–108*, 52–59, doi:10.1016/j.jmarsys.2012.05.010.

Vic, C., G. Roullet, X. Capet, X. Carton, M. J. Molemaker, and J. Gula (2015), Eddy-topography interactions and the fate of the Persian Gulf outflow, *J. Geophys. Res. Oceans*, *120*, 6700–6717, doi:10.1002/2015JC011033.

Waldman, R., et al. (2016), Estimating dense water volume and its evolution for the year 2012–2013 in the north-western Mediterranean Sea: An observing system simulation experiment approach, *J. Geophys. Res. Oceans*, *121*, doi:10.1002/2016JC011694.

Zhong, F., R. Ecke, and V. Steinberg (1991), Asymmetric modes and the transition to vortex structures in rotating Rayleigh-Bénard convection, *Phys. Rev. Lett.*, *67*, 2473–2476, doi:10.1103/PhysRevLett.67.2473.